Dear Editor,

We are writing to express our gratitude for the insightful and constructive comments provided by the reviewers for our manuscript titled *"IMEX_SfloW2D v2: a depth-averaged numerical flow model for volcanic gas-particle flows over complex topographies and water"* (Preprint gmd-2023-80). We are pleased to inform you that we have carefully considered the feedback and suggestions provided by Reviewer 1 and Reviewer 2 and have made substantial revisions to our paper in accordance with their recommendations.

Reviewer 1's comments were particularly insightful, highlighting the need for a more comprehensive discussion of some of the present limits of the model (vertical profiles, settling velocity). In response, we have expanded the Discussion section to provide a more in-depth explanation of these limitations and possible ways to overcome them in future versions. Additionally, Reviewer 1 recommended that the role of sedimentation compared to deposition be better distinguished. To address this, we have changed the terminology used in the manuscript and revised the text to clarify this point.

Reviewer 2's feedback was invaluable in identifying areas where our data analysis and interpretation could be strengthened. Specifically, Reviewer 2 pointed out that for the benchmark 1D tests presented in the work, there are no analytical solutions to prove that the model reproduces them correctly or to help the reader visualize the model's accuracy. As per this suggestion, we have included the equations for the analytical solutions in the manuscript and added the relevant plots to the figures. These changes help to appreciate the accuracy of the numerical model we implemented.

In addition to these major revisions, we have meticulously addressed numerous minor comments and suggestions from both reviewers, ranging from improvements in clarity and coherence to the correction of typographical errors.

We would also like to inform you that one of the authors, Samantha Engwell, is affiliated with the British Geological Survey (BGS). As per the policies of the BGS, all scientific papers authored by BGS employees undergo an internal review process to ensure alignment with institutional guidelines and objectives. For this manuscript, it a landslide expert was engaged from the BGS who suggested additional changes that were made.

We believe that the revisions made in response to the reviewers' feedback have substantially enhanced the quality and impact of our manuscript. We are confident that the changes we have implemented align well with the standards of rigor and clarity that GMD upholds.

Enclosed herewith, please find the detailed answers to all reviewer's comments, the list of new references added to the manuscript, the source of the Matlab script used to compute the analytical solution of the 1D test cases, and a revised version of our manuscript highlighting all the suggested changes. We kindly request that you consider our revised submission for publication in GMD. We would also like to extend our gratitude to the reviewers for their time, expertise, and dedication in helping us improve the quality of our work.

Thank you for considering our revised manuscript. We eagerly await your decision and remain at your disposal for any further information or clarification.

Sincerely,
Mattia de' Michieli Vitturi
Tomaso Esposti Ongaro
Samantha Engwell

Answers to RC1

Q. *Line 20: "...yes, reliable"*

A. The text has been modified as suggested.

Q. *Lines 44-45. Agreed. However, some words should be spent on how a shallow-water model, which by definition cannot solve for vertical gradients of the flow properties, can be employed to simulate DPDCs, which are strongly vertically-stratified (particle concentrantion, flow density, flow velocity).*

A. The following text has been added:

> "In particular, for currents where turbulent mixing is large enough to maintain vertically uniform concentration, shallow water models provide a good approximation (Bonnecaze et al., 1993). This approach can still be used for vertically stratified flows, but it is necessary to introduce appropriate correction factors into the equations, generally based on a simplifying assumption of well-developed and stationary vertical profiles and yet not easy to calculate explicitly (Biagioli et al., 2021; Keim and de' Michieli Vitturi, 2022)."

Q. *Lines 66-74. I agree that entrainment is a key factor controlling DPDCs, however the role of sedimentation should be equally emphasized in this introduction since, like entrainment, it controls the rate of change of the flow bulk density and, hence, its existence. Indeed, some words should be spent in emphasizing the concept that a DPDC, as any other density current (e.g., turbidity currents), exists until there is a density contrast with the ambient in which it flows* **A.** The following text has been modified as follows:

> "On par with entrainment, sedimentation exerts a major role in controlling the rate of change of the flow bulk density and, hence, its existence. Indeed, dilute PDCs, as any other density current (e.g., turbidity currents), exist until there is a positive density contrast with the ambient in which they flow. If sufficient air is entrained or a sufficient amount of particles are lost by sedimentation, then the density falls below that of the ambient air and buoyant liftoff occurs.
>
> The capability of dilute flows to overcome topographic barriers, and consequently the sedimentation regimes, also depends on the Richardson number (Woods and Wohletz, 1991; Woods et al., 1998). For these reasons, an accurate description of these regimes is mandatory for a model of dilute PDCs, both in the definition of the equations and in their numerical discretization and solution."

Q. *Lines 91-92. The repository lacks of a User manual (or at least I cannot find it), which would be very beneficial.*

A. For all the examples provided with the code in the Github repository there is a README file with detailed instruction to create the input files, to run the simulation and to post-process the results.

Q. *Line 104. Is this fixed in the code? Can another gas specie be used? If yes, I would generalize here*

A. The gas component are not fixed, and we tried to make it more clear in the text, by modifying the line indicated by the Reviewer in the following way:

> "we assume that the flow is a homogeneous mixture of a multi-component gas phase (for the applications presented in this work air and water vapour)"

We also added the following text in Section 3.1

"The specific gas constants are provided in the code as user inputs, and more gas can be added, allowing for the simulation of a mixture of any number of gas components."

Q. *Lins 151-152. What are the consequences of this approximation and why is it reasonable to take this into account?*

A. Some of the consequences were already stated before Eq.6 but, to make it more clear, we revised the text and added some references which can provide a more detailed analysis, which is out of the scope of this paper. We report here the revised text (original text from line 138 to 156):

"It is worth noting that the design of conservative and stable numerical schemes for the solution of Eqs. (2-5) requires some care. This is because the numerical solution of mass and momentum equations, even when these quantities are globally conserved, does not necessarily result in an accurate description of the mechanical energy balance of the shallow water system (Fjordholm et al., 2011; Murillo and García-Navarro, 2013). In fact, many numerical schemes perform well in practice but they may have an excessive amount of numerical dissipation near shocks, preventing a correct energy dissipation property across discontinuities (which can arise even in the case of smooth topography). A quantification of the error in the conservation of mechanical energy is beyond the scope of this paper, also because the error is case dependent and the topography plays a crucial role, but the reader can refer to Arakawa and Lamb (1977); Arakawa (1997); Arakawa and Lamb (1981); Fjordholm et al. (2011) for a comprehensive discussion of this issue. In general, to guarantee energy conservation in smooth regimes, it is desirable to design high-order schemes adding a minimal amount of numerical dissipation. Numerical errors in the computation of the mechanical energy can lead to errors associated with the mixture temperature obtained from the total mixture specific energy and the kinetic energy computed from mass and momentum equations. For this reason, in some cases, instead of the full energy equation as presented above, it is preferable to solve a simpler transport equation for the specific thermal energy $C_v T$:

$$\frac{\partial}{\partial t}\left(\rho_m h C_v T\right) + \frac{\partial}{\partial x}\left(C_v T \rho_m h u\right) + \frac{\partial}{\partial y}\left(C_v T \rho_m h v\right) =$$

$$-\sum_{i_s=1}^{n_s}\left(\rho_{s,i_s} C_{s,i_s} T S_{s,i_s}\right) + C_a \rho_a T_a E_a + C_{wv} \rho_{wv,b} T_b E_{wv},$$

We remark that in this equation we neglect heating associated with friction forces. This term can be important for some applications where viscous forces are particularly large, for example lava flows, but are negligible for the applications presented in this work. It is also worth noting that the numerical solution of Eqs. (2-4,6) does not guarantee that the total energy is conserved. In the following section, for simplicity, we use the temperature equation to demonstrate how the system of equations can be written in a more compact form and in the description of the numerical schemes, but for the applications presented in this work the full energy equation is solved."

Q. *Lines 167-168. So, the assumption is made that, everything that is sedimenting is also creating a deposit. This is not always necessarily the case, since sedimenting particles (in fact, I would use a sedimentation term in the conservation equations, instead of a deposition term) can be moved as a traction carpet or even re-entrained.*

A. We thank the reviewer for pointing out that sedimentation does not always result in a deposit. We included the observation of the reviewer in the text, and we also clarified that Eq. 14 is not used in the applications presented in this work, but can be used for different applications. The following text has been added after Eq. 14:

> "This equation assumes that sedimentation of particles immediately results in an increase in deposit thickness, which is not always the case, because particles in the basal layer that forms at the bottom of the flow could be moved as a traction carpet or even re-entrained. While Eq. (14) is appropriate for flows that can be modeled by the system of conservation equations (10), as for example for lahars, it is not used in the application to dilute PDCs presented in this work."

Q. *Lines 169-173. I would further emphasize the strength of IMEX, i.e. the fact that one can choose among 6 different rheological models, hence 6 different ranges of applications, with the same code thanks to the way the model is developed.*

A. The following sentence has been added to the text:

> "This rheological model is available in IMEX_Sflow2D v2, together with a plastic rheology (Kelfoun, 2011), a temperature dependent friction model (Costa and Macedonio, 2005) and a lahar rheology (O'Brien et al., 1993), largely increasing the range of applicability of this version of the code."

Q. *Lines 177-179. As far as I understand reading the manuscript, IMEX is not restricted to radially spreading flows. In my opinion this should be stated more clearly.*

A. We tried to make it more clear modifying the text in the following way:

> "The code we present is mostly aimed at simulating 1D/2D flows, for which we do not simulate the initial phase and, most importantly, for which in radially spreading flows the front velocity decreases because of the increasing radius."

Q. *Line 211. This equation is from Parker et al. (1987), I see the paper is not cited here. https://doi.org/10.1080/00221688709499292 Furthermore, there are other relationships available in the literature, e.g. https://doi.org/10.1029/2003JF000052, https://doi.org/10.1029/2019GL084776. While these should not necessarily be implemented into the code, they can be at least cited perhaps in the introduction when you first introduce the entainment. But at least the model you use should be cited.*

A. We followed the suggestion of the reviewer by adding the suggested references and modifying the text in the following way:

> "where ϵ, following Bursik and Woods (1996), is the entrainment coefficient given by Parker et al. (1987):
>
> $$\epsilon = \frac{0.075}{(1 + 718Ri^{2.4})^{0.5}}. \quad (1)$$
>
> We remark that, even if not implemented in the model, there are other relationships available in the literature for the entrainment coefficient (Ancey, 2004; Dellino et al., 2019a)."

Q. *Lines 226-228. Any reference for this assumption? The larger fraction for smaller particles is reasonable and can perhaps be explained by the larger specific surface (hence, also the type of particles (e.g., pumice vs. lithic fragments) via the shape)*

A. We added the reference Dufek et al. (2007), which provide this estimation.

Q. *Lines 234-237. Sedimentation does not necessarily coincide with deposition. I suggest the authors to review the use of terminology. The models described below and the sink term in the conservation equations are sedimentation rate terms, deposition rates may differ because there may be processes at the deposition interface that mobilize or even re-entrain the particles settling onto the ground. Furthermore, the use of a model like eq. 19 has the limitation that it does not take into account the effect of the flow, specifically the turbulence, on the sedimentation rate. Models like eq. 19 assumes a constant sedimentation rates that does not take into account the turbulence, which can keep particle in suspension. This depends on the Rouse number. See for example the recent works of Dellino et al. (https://doi.org/10.1111/sed.12485, https://doi.org/10.1111/sed.12693) and cited literature therein. I am not implying that the authors should implement these models (which may add a further complexity) but suggesting to make these limitating assumptions clear in the text.*

A. We thanks the reviewer for the comment, and we added the following text at the end of the section:

> "The sedimentation model described by Eq. 19 represents the loss of particles from the flow, but does not necessarily correspond to a deposition rate, i.e. the rate of accretion of deposit thickness. This is true only when the ratio between the actual deposition and the sedimentation rate is high ($> 5 \times 10^{-3}$ according to Shimizu et al., 2019). In fact, there may be processes at the deposition interface that mobilize or even re-entrain the particles settlinginto the concentrated basal layer and then onto the ground. Furthermore, in order not to add further complexity, the adopted equation assumes a constant sedimentation rate which does not take into account the turbulence, which can keep the particles in suspension. A more accurate description of sedimentation based on the Rouse number, representing a ratio of particle settling velocity to scale of turbulence, can be found in (Dellino et al., 2019b, 2020; Valentine, 1987)."

In addition, we changed the notation used for sedimentation from D_{s,i_s} to S_{s,i_s}.

Q. *Lines 241-252. Also here, there are more recent and accurate treatments of the particle settling velocity calculations. For simple spheres (which is a strong and limiting assumptions, see my comments in the following), there are drag laws that avoid the jump in the Lun and Gidaspow drag law (e.g. https://onlinelibrary.wiley.com/doi/10.1002/cjce.5450490403; https://doi.org/10.1016/0032-5910(89)80008-7), which in some situation may cause problems. Then there is the problem of using a drag law for spheres in the case of natural sediments/volcanic particles, which are (very) far from spheres, with strong implications on the Cd and therefore vs. Even if the authors do not want to implement such models (e.g., https://doi.org/10.1016/j.powtec.2018.12.040, https://doi.org/10.1002/2017JB014926, https://doi.org/10.1016/0032-5910(93)80051-B), they should clearly state that their approach is a simplification and that can lead to overestimations of the terminal velocity, hence sedimentation rates in the flow.*

A. We added a paragraph in the section "Conclusion" where the limitations highlighted by the reviewer, together with other limitations, are discussed. We report here the text discussing the settling velocity model:

> "We also point out that the present version of the code implements a rather simplified model for particle settling velocity, and in the future we plan to adopt more recent and accurate treatments for its calculations. For simple spheres, as assumed here, there are drag laws that avoid the jump in the Lun and Gidaspow drag law (Clift and Gauvin, 1971; Haider and Levenspiel, 1989), which can result in numerical problems when the the velocity is computed with an iterative numerical scheme. In addition, the use of a drag law for spheres in the case of natural sediments/volcanic

particles is an important simplification that can lead to overestimation of the terminal velocity, hence the sedimentation rate in the flow. We remark that the adoption of more complex models (Ganser, 1993; Bagheri and Bonadonna, 2016; Dioguardi et al., 2018) would also require the knowledge of additional parameters characterizing the shape of the particles, which are not always easy to retrieve."

Q. *Lines 366-367. Move this to the beginning of the section.*

A. The text has been moved to the beginning of the paragraph.

Q. *Lines 391-392. I suggest moving fig. c under figure a.*

A. The bottom panels have been inverted. In addition, the analytical solutions have been added to the plot to show the accuracy of the numerical solver, together with a legend.

Q. *Lines 497-498. I understand, however I think a complete comparison with a real case, for which data are available, would add more value to the manuscript and the software. The potential user would be more keen to use it for realistic applications. It would be also interesting to see benchmarking applications like comparisons with large-scale experiments, like the experiments carried out recently in New Zealand (PELEE) or the older ones by the University of Bari group. Maybe the former are more complicated for this code, since they produce channelised DPDCs; the latter, though, should be straightforward to reproduce.*

A. Our aim for this paper was to present development of a numerical model for simulating several different types of flows. To demonstrate the capabilities of the model, we chose examples that enabled us to highlight the range of model applications, for example simulating flows over water and flow interaction with topography. While these simulations were informed by real events, they were intended to give the reader insight into the scope of the model capabilities, rather than benchmark the model. With reference to the terminology proposed by Esposti Ongaro et al. (2020), as well as from CFD modeling standards (e.g., Oberkampf and Trucano, 2002) we here focus on the presentation of the model qualification, verification and presentation of unit tests and synthetic benchmarks. We understand the value gained from directly reproducing real events and experiments, but such large- and full-scale benchmark studies are bodies of work in themselves, and are outwith the scope of the paper. In any case, the presented Krakatau runs show the applicability of the code to the natural scale phenomenon. Further work dedicated to the reproduction of flows from the Krakatau 1883 eruption, through application of the model using new, recently collected, grainsize and thickness data from the event is currently in progress. We have changed the text in the abstract, introduction and discussion to highlight that the model has been applied to Krakatau volcano, with model inputs informed by the 1883 eruption, rather than implying that the simulations directly reproduce the eruption.

Q. *Line 499. These are the units of volumetric flow rate.*

A. We changed the units to kg s^{-1}. By double-checking for the units, we also noticed that the reported mass flow rate was wrong and now we reported the correct value (10^{10} kg s^{-1}) in the manuscript.

Q. *Line 500. Space missing.*

A. We added the space.

Q. *Lines 589-590. I expected to see an implementation of the method presented in Biagioli et al. (2021) (https://doi.org/10.1016/j.apm.2020.12.036) in this version of IMEX that allows simulating DPDCs. Is there a reason why this method, that to me looks like a very promising one to take into account vertical profiles in shallow water models, is not taken into account in v2 of IMEX?*

A. The method implemented in Biagioli et al. 2021 focuses on the profiles for Newtonian laminar flow, thus with a parabolic velocity profile, which is not adequate for the turbulent flows considered in this work. In addition, in Biagioli et al. 2021 the flow does not consider the presence of particles. In any case, we agree with the reviewer that the approach presented in

this work is very promising also for other kind of flows, and a similar method has been proposed in Keim and de' Michieli Vitturi (2022), but it is still the object of research. In any case, to account for the comment of the reviewer, we added the following text in the conclusion section:

> "In future versions of the code we plan to adapt an approach similar to that presented for Newtonian laminar flows in (Biagioli et al., 2021), where the depth-average equations have been modified to account for the vertical variation of velocity and temperature. The proposed modifications were implemented in the first version of IMEX-SfloW2D, and the applicability of such approachs to velocity and particle concentration profiles for dilute pyroclastic density currents has been shown in (Keim and de' Michieli Vitturi, 2022)."

Q. *Finally, since this code should guarantee run times compatible with probabilistic volcanic hazard assessments, it would be useful to have some data on the run times vs. used computational resources of a realistic test case (e.g. the presented Krakatau test case).*

A. We added a paragraph in the conclusion section to discuss this point.

> "In conclusion, the depth-averaged model introduced in this study offers a promising avenue for advancing probabilistic volcanic hazard assessment. By providing a computationally efficient alternative to traditional 3D models, it significantly reduces the computational burden while still capturing, as shown by the Krakatau application, essential aspects of volcanic flows. For instance, for the simulation of the Krakatau case study for 1800 seconds, the code required 2 hours of computational time on a 7th Generation Kaby Lake Intel Core i7 processor, which could be substantially reduced with a parallel run on multiple cores. Moreover, the utilization of a High-Performance Computing (HPC) system further amplifies the potential of the depth-averaged model in probabilistic volcanic hazard assessment, enabling the execution of a large number of simulations within a reasonable timeframe. This makes the model well-suited for practical applications where timely hazard assessment is crucial."

Answers to RC2

Q. *Equation 1-4: the notation must be similar. s,is in the equation, sis in the text.*
A. The text has been fixed.

Q. *Line 118: if possible try to avoid the exponent that can be mistaken for "to the b power"*
A. We changed the notation to avoid any confusion.

Q. *Line 143: it's difficult to know whether this simplification has little or a major impact on the results. Under what conditions could induced errors alter the model's results in relation to the natural phenomenon?*

"This can lead to numerical errors associated with the mixture temperature obtained from the total mixture specific energy and the kinetic energy computed from mass and momentum equations. For this reason, in some cases, instead of the full energy equation as presented above, it is preferable to solve a simpler transport equation for the specific thermal energy CvT"

A. This point is important, but a full description of the problem, and a quantification of the error introduced, are out of the scope of this paper, and it is the subject of an active research in the field of the numerical discretization of shallow water equations. In any case, we agree with the reviewer that some additional information should be provided and we have modified the text of the paragraph next to that mentioned by the reviewer in the following way, also providing references for a better comprehension of the problem:

> It is worth noting that the design of conservative and stable numerical schemes for the solution of Eqs. (2-5) requires some care. This is because the numerical solution of mass and momentum equations, even when these quantities are globally conserved, does not necessarily result in an accurate description of the mechanical energy balance of the shallow water system (Fjordholm et al., 2011; Murillo and García-Navarro, 2013). In fact, many numerical schemes perform well in practice but they may have an excessive amount of numerical dissipation near shocks, preventing a correct energy dissipation property across discontinuities (which can arise even in the case of smooth topography). A quantification of the error in the conservation of mechanical energy is beyond the scope of this paper, also because the error is case dependent and the topography plays a crucial role, but the reader can refer to Arakawa and Lamb (1977); Arakawa (1997); Arakawa and Lamb (1981); Fjordholm et al. (2011) for a comprehensive discussion of this issue. In general, to guarantee energy conservation in smooth regimes, it is desirable to design high-order schemes adding a minimal amount of numerical dissipation.

Q. *175: Froude number*
A. Fixed.

Q. *178: "The code we present is mostly aimed at simulating 2D spreading flows, for which we do not simulate the initial phase". Once published and distributed, this code will most likely be used to simulate complete eruptions, including initial phases. Can it be used? Is it possible to quantify the errors if it is used to reproduce the initial phase? Errors of a few percent can be a problem from a mathematical point of view, but are perfectly acceptable in volcanology, where knowledge of source conditions is often limited.*

A. The observation to which the reviewer's comment refers is specific for dilute PDCs. As stated in the manuscript introduction, these kind of flows can form in relation to several volcanic behaviours (Valentine, 1987; Branney and Kokelaar, 2002; Sulpizio et al., 2014; Dufek et al., 2015), including the collapse of Plinian and Vulcanian columns, and the explosive fragmentation of a lava dome or cryptodome (Sigurdsson et al., 2015). To properly describe these source phases, a more complex 3D model would be required, also able to simulate compressible, turbulent flows and non-equilibrium gas-particle dynamics. Inherent to the foundations of the model described

in this work is the assumption that the flow propagates under gravity at the atmospheric pressure, and that the effects of compressibility are negligible. For these reasons, we think that the radial source implemented in the code provides a good initial condition for the propagation of dilute PDCs when they are already at atmospheric conditions, and in particular for flows generated by column collapse of explosive eruptions. For other kind of flows that the model can simulate, but are not presented in this work (landslides, pyroclastic avalanches, lahars, lava flows), the code provides different kinds of initial conditions, which allows simulation of the complete event. In the code repository, the Etna test case provides an example of a pyroclastic avalanche where the flow is generated by the collapse of a crater.

Q. *Equation 16 / line 125: Something is not clear to me. Is the entrainment calculated only on the edges or in the whole flow? From equation 16, it seems that entrainment also takes place within the flow itself. In that case, the hypothesis of line 125 does not seem right to me because the flow carries momentum: "There are no terms associated with air and water vapour entrainment, because they do not carry any horizontal momentum into the flow."*

A. Both air entrainment and water vapour entrainment take place at the interfaces between the flow and the entrained gases. Thus, air entrainment occurs over the whole top surface of the flow, while water vapor entrainment occurs at the bottom surface, when in contact with the sea surface. Entrainment, as any other exchange with external medium, results in mass, momentum and energy exchanges, because the mass, momentum and energy "possessed" before the entrainment "enter" into the flow. But, for both atmospheric air and water vapour, the velocity before entraiment is null, and thus no momentum is added to the flow with entrainment. With regards to energy, no kinetic energy is added, while the thermal energy of entrained air and water vapour increase the total energy of the flow.

Q. *They way chosen to define the Ridchardson number is close to a Froude number (Ri = 1/Fr^2). I am a bit lost to see the link with the ratio of the stabilizing stratification of the current to destabilizing velocity shear and, consequently, with the entrainment."*

A. The reviewer is correct in the relationship he wrote about the Richardson number and the Froude number. We will try to explain here why the Richardson number also quantify the balance between the stabilizing effects of stratification (variation of density with height) and the destabilizing effects of velocity shear (variation of velocity with height) in a fluid flow, thus providing insight into the stability characteristics of the flow and is particularly relevant in situations involving buoyancy forces, such as in the atmosphere and oceans.

To make it more clear we first observe that the Richardson number can be written also in the following equivalent form:

$$Ri = \frac{g}{\rho}\frac{\Delta\rho}{\Delta z}\left(\frac{\Delta u}{\Delta z}\right)^{-2}$$

where:

- g is the acceleration due to gravity.
- ρ is the density of the fluid.
- $\Delta\rho$ is the change in density across a certain distance Δz in the vertical direction.
- Δu is the change in horizontal velocity across the same distance Δz.

Now, let's break down the relationship between the Richardson number and the stabilizing stratification of the current versus destabilizing velocity shear:

1. *Stabilizing Stratification*: When there is a stable stratification, it means that denser fluid is located below lighter fluid, creating a situation where lighter fluid tends to rise over denser fluid due to buoyancy forces. In other words, the density gradient ($\Delta\rho/\Delta z$) in the denominator of the Richardson number quantifies the stabilizing effect of stratification. If this gradient is large (strong stratification), it indicates that the buoyancy forces are significant, and the flow is less likely to become turbulent or mixed due to the upward tendency of the lighter fluid.

2. *Destabilizing Velocity Shear*: Velocity shear refers to the change in velocity across a distance. If there is a significant change in horizontal velocity ($\Delta u/\Delta z$) across the same distance

Δz, it can lead to velocity shear, which can induce mixing and turbulence in the flow. Velocity shear is often associated with the destabilizing effects that can disrupt the stability imposed by stratification.

The relationship between these two aspects becomes apparent when you examine the Richardson number. A large Richardson number (indicating strong stratification relative to velocity shear) means that the stabilizing effects of buoyancy forces dominate over the destabilizing effects of velocity shear. This leads to a more stable flow with less mixing and turbulence, thus a reduced entrainment.

Conversely, a small Richardson number (indicating weak stratification relative to velocity shear) implies that the destabilizing effects of velocity shear are strong enough to overcome the stabilizing effects of buoyancy forces. This can result in increased mixing, turbulence, and enhanced entrainment.

In the manuscript, we tried to summarize what is written above in the following way:

> "As the flow propagates, air is entrained at a rate which: (i) is proportional to the magnitude of the difference in velocity between the flow and the stationary ambient; and (ii) depends on the ratio of the stabilizing stratification of the current ($N^2 = \frac{g}{\rho}\frac{\Delta\rho}{\Delta z}$, where N is the Brunt-Väisälä frequency) to destabilizing velocity shear ($M^2 = \left(\frac{\Delta u}{\Delta z}\right)^{-2}$, where M is also called the the Prandtl frequency). This ratio is expressed by the Richardson number (Cushman-Roisin and Beckers, 2011) and, following Bursik and Woods (1996), is written in the following equivalent form:
>
> $$Ri = g'h/(u^2 + v^2), \tag{2}$$
>
> where g' is the reduced gravity. Written in this form, this is essentially a ratio between between potential and kinetic energies, with the numerator being the potential energy needed to entrain the overlying buoyant fluid and the denominator being the kinetic energy of the flow which cause this entrainment."

Following the suggestion of Reviewer 1, we also added a reference for Eq. 17 (Parker et al., 1987). This reference can help to better understand the relationship between entrainment and the Richardson number.

Q. *289: Could the authors explain what is an "opportune slope limiter"? On what criteria are they chosen? This choice seems to have strong consequences on edge values and therefore on the fluxes.*

A. We added the following text to the manuscript:

> "Slope limiters are employed to mitigate the occurrence of excessive oscillations and unrealistic behavior that might arise during the solution of partial differential equations through finite volume methods, especially in proximity to shocks and discontinuities. When prioritizing accurate shock representation, the Superbee slope limiter can be the best choice as it maintains sharper discontinuities, but at the cost of a tendency of smooth humps to become steeper and squared with time. If preserving monotonicity and minimizing oscillations in smooth regions are more important, then MinMod could be favored. For a more detailed analysis of slope limiters and finite volume methods, the reader can refer to LeVeque (2002)."

Q. *Figure 1: The authors use two flux values, Q(w, j-1, k) and Q(E, j, k) for example. What is the physical reality of these two flows at the same location? I didn't understand whether there was a procedure to make them compatible.*

Line 311: same question here. I wonder if it's physically correct to consider 2 speeds, one to the left, the other to the right, in the same place? Is this choice linked to the physics of the phenomenon or to numerical stability?

A. Having two different values at the two sides of interfaces in a numerical method, such as finite volume methods or finite difference methods, might seem counterintuitive from a physical standpoint, as it doesn't directly reflect the smooth nature of many real-world physical phenomena. However, this discrepancy is a consequence of the mathematical discretization process used in numerical methods to approximate continuous partial differential equations (PDEs) over discrete domains.

In particular, having two values at the two sides of interfaces in finite volume methods (FVM) is essential for properly describing and capturing discontinuous solutions. Discontinuities are abrupt changes or jumps in the solution variables, such as shock waves, interfaces between different materials, or other sharp transitions in physical phenomena. Finite volume methods are designed to handle these types of phenomena, and the presence of two values at cell interfaces contributes to their accuracy in representing such solutions.

Here's how:

- *Accuracy at Discontinuities*: Discontinuities are inherently present in many physical processes, and they need to be accurately captured by numerical methods. Having two different values at the cell interfaces allows FVM to represent the abrupt changes in solution variables, such as density, pressure, or concentration, which occur at these discontinuities.

- *Numerical Fluxes*: FVM calculates numerical fluxes, which represent the flow of quantities across cell interfaces. These fluxes are based on the differences between the values at the two sides of the interface. By incorporating both values, FVM can construct more accurate approximations of how the solution changes across the discontinuity.

- *Shock Capturing*: One of the main strengths of FVM is its ability to effectively capture and resolve shock waves. Shock waves are characterized by steep gradients and rapid changes in solution variables. The presence of two values at the interfaces allows FVM to accurately compute fluxes and gradients, capturing the sharpness of the shock profile.

- *Limiters*: In the presence of steep gradients, slope limiters (as mentioned earlier) control oscillations and ensure the accuracy of the solution. These limiters often use information from both sides of the interface to determine how to adjust gradients and avoid unphysical oscillations.

- *Convergence and Conservation*: Properly resolving discontinuities is crucial for the convergence of the numerical solution to the correct physical solution. FVM's focus on conservation principles within control volumes helps maintain the integrity of these abrupt changes.

In summary, having two values at the two sides of interfaces in finite volume methods is indeed crucial for describing and capturing discontinuous solutions accurately. It allows FVM to effectively handle sharp gradients, shock waves, and other abrupt changes in solution variables that are characteristic of real-world physical phenomena.

To make this clearer in the manuscript, we summarized the above text in the following way in the paper:

> "Having two different values at the two sides of interfaces in a numerical method might seem counterintuitive from a physical standpoint. However, this jump is a consequence of the mathematical discretization process used in the finite volume method to approximate continuous partial differential equations (PDEs) over discrete domains. In particular, having two values at the two sides of interfaces in finite volume methods is essential for properly describing and capturing discontinuous solutions."

Q. *Lines 325-327: I'm not able to understand what these choices imply for the model's results.*

A. We added the following text to the manuscript:

> "The implicit treatment of the friction terms, when dealing with strongly non-linear rheologies, avoids many problems related to the proper stopping condition of the flow, without the need for introducing arbitrary thresholds. In addition, the automatic derivation of the friction term allows for a simple implementation of any rheological model, including formulations dependent on any model parameter."

Q. *Figure 2: captions d and c are inversed.*

A. The figure has been fixed.

Q. *Figure 2, 3, 4... : if I'm not mistaken, the proposed solutions are only those of the model. Is there no analytical solution to prove that the model reproduces them correctly or to help the reader visualize the model's precision? How do the reader know if the model is working properly?*

A. We added in the manuscript the equations for the analytical solutions of test cases shown in Figures 2 and 3, and the relative profiles have been added to the Figures. We report here the text added to the manuscript.

> "By integrating equation 30 with the additional condition of constant volumetric flux (as expressed by the first of Eqs. 28) we also have, in the case of a regular solution, the following Bernoulli relation:
>
> $$\frac{(hu)^2}{2g'h^2} + h + z = Const, \tag{3}$$
>
> which gives us a relation between the topography elevation and the flow height. Using Eq. 30, in the cases of supercritical or subcritical flows without regime transitions, it is possible to obtain the following implicit equation for the flow depth (Delestre et al., 2013):
>
> $$h(x)^3 + \left(B(x) - \frac{(h_0 u_0)^2}{2g'h_0^2} \right) h(x)^2 + \frac{(h(x)u(z))^2}{2g'} = 0, \tag{4}$$
>
> where h_0 is the flow thickness at the inlet or outlet of the domain."

Similar text has been added after the description of the transcritical test case, with and without shock. Furthermore, a Matlab script to compute and plot the analytical solution is provided in this document after the list of new references.

Q. *Figure 10 (13 and the others): if possible, change the curve lines to adapt them to black and white printing*

A. We changed the line patterns in figure 13 to adapt them to black and white. For Figures 10 and 11 this was not easy to do, because of the large number of lines plotted. If the editor thinks it necessary, we can add each of the individual profiles as separate figures in the Supplementary material.

Q. *Figure 13: why at the source, the entrained air represents 100% of the gases? Can't you distinguish between air initially present and entrained air? The scale does not seem right for the low particle concentration. Perhaps a more specific scale on the right-hand axis would be more appropriate.*

A. As explained above, the source does not the correspond to the vent, but to the radial flow of the already decompressed mixture, resulting from the collapse of the explosive column.

In this initial phase, which we do not simulate, a lot of atmospheric air is entrained, and this is why the particle concentration is low. In any case, we want to point out that at the source of the simulated dilute flow, the entrained air does not represent 100% of the gases, because a small amount is also represented by the volcanic gas (here water vapour). To make it clearer that the initial condition refers to source of the radially spreading flow, and not to vent conditions, we added the following text to the manuscript:

> We point out that we do not simulate here the collapse of the explosive column, but only the dilute flow generated by the entrainment of atmospheric air and the collapse of the column. Thus, the initial conditions of the simulation refers to the source conditions of the radially spreading dilute flow.

Q. *Line 500 and 365: kg m-3 (with a space)*
A. The notation has been fixed.

List of new references

Ancey, C.: Powder snow avalanches: Approximation as non-Boussinesq clouds with a Richardson number–dependent entrainment function, Journal of Geophysical Research: Earth Surface, 109, 2004.

Arakawa, A.: Computational design for long-term numerical integration of the equations of fluid motion: Two-dimensional incompressible flow. Part I, Journal of computational physics, 135, 103–114, 1997.

Arakawa, A. and Lamb, V. R.: Computational design of the basic dynamical processes of the UCLA general circulation model, General circulation models of the atmosphere, 17, 173–265, 1977.

Arakawa, A. and Lamb, V. R.: A potential enstrophy and energy conserving scheme for the shallow water equations, Monthly Weather Review, 109, 18–36, 1981.

Bagheri, G. and Bonadonna, C.: On the drag of freely falling non-spherical particles, Powder Technology, 301, 526–544, 2016.

Bonnecaze, R. T., Huppert, H. E., and Lister, J. R.: Particle-driven gravity currents, Journal of Fluid Mechanics, 250, 339–369, 1993.

Clift, R. and Gauvin, W.: Motion of entrained particles in gas streams, The Canadian Journal of Chemical Engineering, 49, 439–448, 1971.

Cushman-Roisin, B. and Beckers, J.-M.: Introduction to geophysical fluid dynamics: physical and numerical aspects, Academic press, 2011.

Delestre, O.: Simulation du ruissellement d'eau de pluie sur des surfaces agricoles, Ph.D. thesis, Université d'Orléans, 2010.

Dellino, P., Dioguardi, F., Doronzo, D. M., and Mele, D.: The entrainment rate of non-Boussinesq hazardous geophysical gas-particle flows: An experimental model with application to pyroclastic density currents, Geophysical Research Letters, 46, 12 851–12 861, 2019a.

Dellino, P., Dioguardi, F., Doronzo, D. M., and Mele, D.: The rate of sedimentation from turbulent suspension: An experimental model with application to pyroclastic density currents and discussion on the grain-size dependence of flow runout, Sedimentology, 66, 129–145, 2019b.

Dellino, P., Dioguardi, F., Doronzo, D. M., and Mele, D.: A discriminatory diagram of massive versus stratified deposits based on the sedimentation and bedload transportation rates. Experimental investigation and application to pyroclastic density currents, Sedimentology, 67, 2013–2039, 2020.

Dioguardi, F., Mele, D., and Dellino, P.: A new one-equation model of fluid drag for irregularly shaped particles valid over a wide range of Reynolds number, Journal of Geophysical Research: Solid Earth, 123, 144–156, 2018.

Esposti Ongaro, T., Cerminara, M., Charbonnier, S.J. et al. A framework for validation and benchmarking of pyroclastic current models. Bull Volcanol 82, 51 (2020). https://doi.org/10.1007/s00445-020-01388-2

Ganser, G. H.: A rational approach to drag prediction of spherical and nonspherical particles, Powder technology, 77, 143–152, 1993.

Haider, A. and Levenspiel, O.: Drag coefficient and terminal velocity of spherical and nonspherical particles, Powder technology, 58, 63–70, 1989.

Keim, B. and de' Michieli Vitturi, M.: Implementation of Vertical Profiles for Velocity and Particle Concentration Into a 2D, Depth-Averaged Model for Dilute Pyroclastic Density Currents, in: AGU Fall Meeting Abstracts, vol. 2022, pp. V52C–0017, 2022.

Kelfoun, K.: Suitability of simple rheological laws for the numerical simulation of dense pyroclastic flows and long-runout volcanic avalanches, Journal of Geophysical Research: Solid Earth, 116, 2011.

LeVeque, R. J.: Finite volume methods for hyperbolic problems, vol. 31, Cambridge university press, 2002.

Parker, G., Garcia, M., Fukushima, Y., and Yu, W.: Experiments on turbidity currents over an erodible bed, Journal of Hydraulic Research, 25, 123–147, 1987.

Shimizu, H. A., Koyaguchi, T. and Suzuki, Y. J. (2023). Dynamics and deposits of pyroclastic density currents in magmatic and phreatomagmatic eruptions revealed by a two-layer depth-averaged model. Geophysical Research Letters, 50, e2023GL104616.

Matlab script for analytical solutions

```
close all
clear all

L = 25;

nx = 2000;

x = linspace(0,L,nx);

% topography
zM = 0.2;
z = 0*x + (x>8).*(x<12).*(zM-0.05*(x-10).^2);

g = 9.81;

%% subcritical solution
figure;
subplot(2,1,1)
plot(x,z)


q0 = 4.42;
hL = 2;

h_sub = 0*x;

for i=1:nx,

    h_set = roots([1,(z(i)-q0^2/(2*g*hL^2)-hL),0,q0^2/(2*g)]);
    [minValue,closestIndex] = min(abs(h_set-hL));
    h_sub(i) = h_set(closestIndex);

end

hold all
plot(x,z+h_sub);
xlim([0,25])
ylim([-0.10,2.1])

subplot(2,1,2);
plot(x,q0./h_sub)

xlim([0,25])
ylim([2.191,2.6072])


%% supercritical solution

figure;
subplot(2,1,1)

plot(x,z)

q0 = 10;
hL = 1;

h_sup = 0*x;

for i=1:nx,

    h_set = roots([1,(z(i)-q0^2/(2*g*hL^2)-hL),0,q0^2/(2*g)]);
```

```
    [minValue,closestIndex] = min(abs(h_set-hL));
    h_sup(i) = h_set(closestIndex);

end

hold all
plot(x,z+h_sup);
xlim([0,25])
ylim([-0.10,1.3])

subplot(2,1,2);
plot(x,q0./h_sup)
xlim([0,25])
ylim([9.7688,10.01])


%% transcritical without shock

figure;
subplot(2,1,1)

plot(x,z)

q0 = 1.53;
hL = 0.66;

h_trans = 0*x;

hC = (q0/sqrt(g))^(2/3);

hOLD = 1.01;

for i=1:nx,

    h_set = roots([1,(z(i)-q0^2/(2*g*hC^2)-hC-zM),0,q0^2/(2*g)]);
    if x(i) < 10
        [minValue,closestIndex] = min(abs(h_set-hOLD));
    else
        [minValue,closestIndex] = min(abs(h_set-(hOLD-0.1)));
    end
    h_trans(i) = h_set(closestIndex);
    hOLD = h_trans(i);

end

hold all
plot(x,z+h_trans);
xlim([0,25])
ylim([-0.10,1.1])

subplot(2,1,2);
plot(x,q0./h_trans)
xlim([0,25])
ylim([1.39,3.88])


%% transcritical wit shock

figure;
subplot(2,1,1)

plot(x,z)

```

```
q0 = 0.18;
hL = 0.33;

h_trans = 0*x;
h1 = 0*x;
h2 = 0*x;

hC = (q0/sqrt(g))^(2/3);

hOLD = 0.4;

fVal = 0*x;

for i=1:nx,

    x(i)
    h_set = roots([1,(z(i)-q0^2/(2*g*hC^2)-hC-zM),0,q0^2/(2*g)])
    if x(i) < 10
        [minValue,closestIndex] = min(abs(h_set-hOLD));
    else
        [minValue,closestIndex] = min(abs(h_set-(hOLD-0.1)));
        [minValue,closestIndex] = max(h_set);
        closestIndex = 2;
    end
    h1(i) = h_set(closestIndex);
    hOLD = h1(i);

    h_set2 = roots([1,(z(i)-q0^2/(2*g*hL^2)-hL),0,q0^2/(2*g)]);

    [minValue,closestIndex] = min(abs(h_set2-hL));
    h2(i) = h_set2(closestIndex);

    if x(i)<10

        fVal(i) = 1.0;
    else

        fVal(i) = q0^2*(1/h1(i)-1/h2(i))+g/2*(h1(i)^2-h2(i)^2);

    end

end

[minValue,closestIndex] = min(abs(fVal));

x_shock = x(closestIndex);

for i=1:nx,

    if x(i)<=x_shock
        h_trans(i)=h1(i);
    else
        h_trans(i)=h2(i);
    end

end

hold all
plot(x,z+h_trans);
xlim([0,25])
ylim([-0.05,0.5])

subplot(2,1,2);
```

```
plot(x,q0./h_trans)
xlim([0,25])
ylim([0.339,2.43])
```

IMEX_SfloW2D v2: a depth-averaged numerical flow model for volcanic gas-particle flows over complex topographies and water

Mattia de' Michieli Vitturi[1], Tomaso Esposti Ongaro[1], and Samantha Engwell[2]

[1]Istituto Nazionale di Geofisica e Vulcanologia, Sezione di Pisa, Pisa, Italy
[2]British Geological Survey, The Lyell Centre, Research Avenue South, Edinburgh, UK

Correspondence: Mattia de' Michieli Vitturi (mattia.demichielivitturi@ingv.it)

Abstract. We present developments to the physical model and the open source numerical code IMEX_SfloW2D (de' Michieli Vitturi et al., *Geosci. Mod. Devel.*, 2019). These developments consist of a generalization of the depth-averaged (shallow-water) fluid equations to describe a polydisperse fluid-solid mixture, including terms for sedimentation and entrainment, transport equations for solid particles of different sizes, transport equations for different components of the carrier phase, and an equation for temperature/energy. Of relevance for the simulation of volcanic mass flow, vaporization and entrainment of water are implemented in the new model. The model can be easily adapted to simulate a wide range of volcanic mass flows (pyroclastic avalanches, lahars, pyroclastic surges) and here we present its application to transient dilute pyroclastic density currents (PDCs). The numerical algorithm and the code have been improved to allow for simulation of sub- to supercritical regimes and to simplify the setting of initial and boundary conditions. The code is open-source. The results of synthetic numerical benchmarks demonstrate the robustness of the numerical code in simulating trans-critical flows interacting with the topography. Moreover, they highlight the importance of simulating transient in comparison to steady-state flows, and flows in 2D versus 1D. Finally, ~~simulation of the Krakatau 1883 eruption demonstrates the capability of the numerical model to face~~ we demonstrate the model capabilities to simulate a complex natural case involving the propagation of PDCs over the sea surface and across topographic obstacles, through application to Krakatau volcano, showing the relevance, at the large scale, of non-linear fluid dynamic features, such as hydraulic jumps and Van Karman vortexes to flow conditions such as velocity and runout.

1 Introduction

In the past decades, the development of numerical models for geophysical mass flows and their application to hazard assessment has seen a rapid growth. Better understanding of the physics governing such flows has enabled development of more accurate models while a tremendous increase in computational resources has made increasingly high-resolution numerical simulations possible. Despite these advances, for some applications, there is still the need for simplified and fast, yet reliable, models. This is true, for example, for forecasting and hazard quantification purposes, where a probabilistic approach generally requires a large number (thousands or more) of simulations in a relatively short time frame.

For a large class of geophysical mass flows, characterized by having the horizontal length scale much greater than vertical one, it is possible to reduce the dimensionality of the problem (and thus the computational cost of its numerical solution) by adopting the so-called Shallow Water Equations approach. The shallow-water equations are a set of partial differential equations that describe fluid flow problems, originally introduced by Adhemar Jean Claude Barre de Saint-Venant, obtained by the averaging of ~~a flows~~ flow variables over its thickness, thus reducing the model complexity (Pudasaini and Hutter, 2007; Toro, 2013). Shallow-water equations have been applied successfully to tsunamis (Fernández-Nieto et al., 2008), atmospheric flows (Zeitlin, 2018), storm surges (Von Storch and Woth, 2008), landslides and debris flows (Iverson and Denlinger, 2001; Denlinger and Iverson, 2001), snow and rock avalanches (Bartelt et al., 1999; Christen et al., 2010) and planetary flows (Iga and Matsuda, 2005). In the volcanological field, shallow-water equations have been applied to the umbrella cloud spreading (Johnson et al., 2015; de' Michieli Vitturi and Pardini, 2021), lahars (Fagents and Baloga, 2006; O'Brien et al., 1993), pyroclastic density currents (Pitman et al., 2003; Patra et al., 2005; Capra et al., 2008; Calabrò et al., 2022; Kelfoun et al., 2009; de' Michieli Vitturi et al., 2019; Shimizu et al., 2017a) and lava flows (Costa and Macedonio, 2005; Biagioli et al., 2021; Hyman et al., 2022).

Another common feature of most geophysical flows is that they are multiphase flows, with a continuous carrier phase (gas or liquid) and a solid dispersed phase. For the numerical modeling of such multiphase flows two main approaches can be adopted, with the solid phase treated as a continuum (Eulerian approach) or as discrete elements for which the equations of motion are solved (Lagrangian approach). The latter approach is better suited for low particle concentration and when the particle relaxation time, quantifyied by the inertial effect of particles, is much smaller than the characteristic time of collisions between particles (Dufek, 2015; Neri et al., 2022). For the volcanological applications of interest here (dilute pyroclastic density currents, or ~~PDC~~dilute PDCs), the flow can be highly turbulent favouring particle collisions, and thus the continuum approach is appropriate. Most of these flows can be described and modeled using the full 3D transient multiphase Navier-Stokes equations but, since the numerical three-dimensional calculation is still very costly, it makes sense to reduce the equations for calculations with simpler flow conditions. In particular, for currents where turbulent mixing is large enough to maintain vertically uniform concentration, shallow water models provide a good approximation (Bonnecaze et al., 1993). This approach can still be used for vertically stratified flows, but it is necessary to introduce appropriate correction factors into the equations, generally based on a simplifying assumption of well-developed and stationary vertical profiles and yet not easy to calculate explicitly (Biagioli et al., 2021; Keim and de' Michieli Vitturi, 2022).

In this work, we present a new version of IMEX-SfloW_2D (de' Michieli Vitturi et al., 2019), a depth-averaged model originally developed for the simulation of pyroclastic avalanches, i.e. a type of granular flow characterized by relatively thin layers at high particle concentration (10–50 vol %). Similarly to other codes used in volcanological research and applications such as Volcflow (Kelfoun and Druitt, 2005), TITAN2D (Pitman et al., 2003; Patra et al., 2005), and SHALTOP (Bouchut and Westdickenberg, 2004; Mangeney et al., 2007), IMEX-SfloW_2D is a shallow-water equations model based on depth-averaging, obtained by integrating the full 3D equations along the vertical dimension. With respect to the original version of the model (de' Michieli Vitturi et al., 2019), where the granular mixture was described as a single-phase mono-disperse granular fluid ignoring the presence of the interstitial gas, here the formulation and the equations have been generalized to a

fluid-solid mixture, also adding sedimentation and entrainment terms, transport equations for the solid particles of different sizes, transport equations for different components of the carrier phase, and an equation for temperature/energy.

The model framework is general and, by changing the constitutive equations defining phase properties and flow rheology, it is possible to simulate a variety of geophysical flows. However, in this paper we focus our attention on the modeling of PDCs, i.e. flows of gas and pyroclasts (fragments of volcanic rocks produced by explosive fragmentation), and in particular dilute PDCs, which are characterized by densities of less than 10 kg/m^3 (roughly corresponding to a particle volume fraction of less than approximately 0.01). This hypothesis allows us to neglect the influence of particle-particle friction and the internal stress tensor.

Dilute PDCs can form in relation to several volcanic behaviours (Valentine, 1987; Branney and Kokelaar, 2002; Sulpizio et al., 2014; Dufek et al., 2015), including the collapse of Plinian and Vulcanian columns, and the explosive fragmentation of a lava dome or cryptodome (Sigurdsson et al., 2015). Irrespective of the generating mechanism, dilute PDC propagation regimes can be characterized by the flow Richardson number (Ri), expressing the ratio between the potential energy and the kinetic energy available for mixing or, in other terms, the ratio between the relative celerity of surface waves and the velocity of the flow (Chow, 1959). Dilute PDCs may propagate as either subcritical ($Ri > 1$) or supercritical ($Ri < 1$) flows (Bursik and Woods, 1996), and they can also experience transitions from one regime to the other. For supercritical flows, where the speed of the flow is greater than the speed of gravity waves, entrainment is significant and the runout distance tends to be shorter. As large amounts of ambient air are entrained into the flow, ash particles elutriate to form a coignimbrite column (Bursik and Woods, 1996; Engwell et al., 2016). Conversely, subcritical flows, where the velocity of the flow is low enough for internal waves to propagate in either direction, have negligible entrainment and tend to have longer runout distances. On par with entrainment, sedimentation exerts a major role in controlling the rate of change of the flow bulk density and, hence, its existence. Indeed, dilute PDCs, as any other density current (e.g., turbidity currents), exist until there is a positive density contrast with the ambient in which they flow. If sufficient air is entrained or a sufficient amount of particles are lost by sedimentation, then the density falls below that of the ambient air and a buoyant liftoff occurs. The capability of dilute flows to overcome topographic barriers, and consequently the sedimentation regimes, also depends on the Richardson number (Woods and Wohletz, 1991; Woods et al., 1998). For these reasons, an accurate description of these regimes is mandatory for a model of dilute PDCs, both in the definition of the equations and in their numerical discretization and solution.

In this work, Sections 2 and 3 are devoted to the presentation of the new physical model for dilute PDCs based on the shallow-water approximation. The new model extends previous similar models by describing a polydisperse fluid-solid mixture with sedimentation and entrainment terms, transport equations for the solid particles of different sizes, transport equations for different components of the carrier phase, and an equation for temperature/energy. Moreover, it accounts for the potential vaporization of liquid water and entrainment of water vapour into the current. Section 4 summarizes the main aspects of the numerical algorithm, with emphasis on those details that are relevant for resolving the sub- supercritical transitional regimes. We devote Section 5 to the application of the model to one-dimensional literature benchmark tests (Delestre et al., 2013), in order to show the capability of the code to properly simulate the different flow regimes. For supercritical conditions, we also present two 2D test cases, derived from Engwell et al. (2016). These tests show that the steady conditions reached by the

simulation after the initial transient phase correspond to those obtained with the 1D steady model presented in Engwell et al. (2016) and based on Bursik and Woods (1996). Finally, in Section 6 the model is applied to Krakatau volcano, with input parameters informed by the 1883 ~~Krakatau~~ eruption. This is an original study on the propagation of PDCs over water, with a complex 3D topography and display of complex super/subcritical regime transitions, well representing the complexity of PDC dynamics in real cases. For this example, a 30m SRTM DEM of the area is used, which allows us to simulate the effects of real topographic obstacles on the flow propagation and understand how they control the flow regime.

Most of the examples presented in this work, as well as the source code, can be freely downloaded from the model repository at github.com/demichie/IMEX_SfloW2D_v2. The Github repository also contains pre- and post-processing Python scripts, both general and specific for the included examples. The repository and the codes (Fortran main code and Python utility scripts) are compliant with the set of standards defined by the European Open Science Cloud (EOSC) Synergy (SQAaas gold badge) which assigned, through a Quality Assessment & Awarding (QAA), a SQAaas Gold Badge. The compiled code is also available as a Docker container at the following link: hub.docker.com/r/demichie/imex_sflow2d_v2.

2 The physical model

We describe here the equations adopted to describe a gas-particle flow with temperature-dependent mixture density, under the assumption that the flow propagates at atmospheric pressure, and that the effects of compressibility are negligible. In addition, we adopt a physical formulation based on depth averaging of the flow variables, which is appropriate for shallow flows and is computationally less expensive than considering density and velocity variation with depth.

The model is based on the Saint-Venant equations (Pudasaini and Hutter, 2007; Toro, 2013), coupled with source terms describing the entrainment/loss of mass and frictional forces, and enriched with an energy equation and with transport equations for different flow phases/components. In fact, we assume that the flow is a homogeneous mixture of a multi-component gas phase (for the applications presented in this work air and water vapour) and n_s dispersed solid phases. The density of the mixture $\rho_m(x,y,t)$ is defined in terms of the volumetric fractions $\alpha_{(\cdot)}$ and densities $\rho_{(\cdot)}$ of the components:

$$\rho_m = \alpha_a \rho_a + \alpha_{wv} \rho_{wv} + \sum_{i_s=1}^{n_s} \alpha_{s,i_s} \rho_{s,i_s}, \tag{1}$$

where the subscript a denotes the air component, the subscript wv denotes the water vapour component, and the subscript ~~s_{i_s}~~ s,i_s denote the class $i_s = 1,\dots,n_s$ of the solid phases. Each solid class is characterized by its diameter d_{i_s}, density ρ_{s,i_s}, and specific heat C_{s,i_s}. For a full list of model variables and notation, please refer to Table 1.

Equations are written in global Cartesian coordinates, with x and y orthogonal to the $z-$axis, parallel to gravitational acceleration $\mathbf{g} = (0,0,g)$. We denote the flow thickness (parallel to the vertical $z-$axis) with $h(x,y,t)$ and the horizontal components of the flow velocity with $u(x,y,t)$ and $v(x,y,t)$ (averaged over the vertical flow thickness). The flow moves over a topography $B(x,y,t)$, and we allow the topography to change with time (for example, by particle sedimentation).

Conservation of mass for the flow is calculated:

$$\frac{\partial \rho_m h}{\partial t} + \frac{\partial (\rho_m h u)}{\partial x} + \frac{\partial (\rho_m h v)}{\partial y} = -\sum_{i_s=1}^{n_s} [\rho_{s,i_s} D_{s,i_s})]^{n_s} [\rho_{s,i_s} S_{s,i_s})] + \rho_a E_a + \rho^b_{wv} {}_{wv,b} E_{wv}, \quad (2)$$

where ~~D_s~~ S_s is the volumetric rate of ~~deposition~~ sedimentation of solid particles, E_a is the volumetric air entrainment rate from the atmosphere, and E_{wv} is the volumetric water vapour entrainment, which could occur for flows over water bodies (sea or lakes). These rates are defined per unit surface area, and thus have units ms^{-1}. ~~We assume that the density ρ^b_{wv}~~ The notation $\rho_{wv,b}$ used here denotes the density of water vapour ingested into the flow, which is not that corresponding to flow temperature, but at boiling temperature.

Introducing the notation g' for the reduced gravity $g' = [(\rho_m - \rho_a)/\rho_m]g$, the equations for the momentum components are:

$$\frac{\partial (\rho_m h u)}{\partial t} + \frac{\partial}{\partial x}\left(\rho_m h u^2 + \rho_m g' \frac{h^2}{2}\right) + \frac{\partial}{\partial y}(\rho_m h u v) = -\rho_m g' h \frac{\partial B}{\partial x} + F_x - u \sum_{i_s=1}^{n_s} (\rho_{s,i_s} D S_{s,i_s}), \quad (3)$$

$$\frac{\partial (\rho_m h v)}{\partial t} + \frac{\partial}{\partial x}(\rho_m h u v) + \frac{\partial}{\partial y}\left(\rho_m h v^2 + \rho_m g' \frac{h^2}{2}\right) = -\rho_m g' h \frac{\partial B}{\partial y} + F_y - v \sum_{i_s=1}^{n_s} (\rho_{s,i_s} D S_{s,i_s}), \quad (4)$$

where F_x and F_y represent the friction terms. Eqs. ~~3 and 4~~ (3) and (4) are derived in the so-called hydrostatic approximation, i.e., the variation of momentum in the z direction are neglected and pressure is always hydrostatic.There are no terms associated with air and water vapour entrainment, because they do not carry any horizontal momentum into the flow.

Density of the gas components is a function of the flow temperature T, which changes with entrainment of external air. In addition, part of the thermal energy of particles lost when the current travels over water produces steam which can be entrained in the flow. For this reason, with respect to the classical incompressible shallow water equations, we also model the total energy budget of the flow, by solving the following equation for the total mixture energy (sum of internal and kinetic energies):

$$\frac{\partial}{\partial t}\left[\rho_m h \left(C_v T + \frac{1}{2}(u^2 + v^2)\right)\right] + \frac{\partial}{\partial x}\left(\left[C_v T + \frac{1}{2}(u^2 + v^2) + g' \frac{h}{2}\right] \rho_m h u\right)$$

$$+ \frac{\partial}{\partial y}\left(\left[C_v T + \frac{1}{2}(u^2 + v^2) + g' \frac{h}{2}\right] \rho_m h v\right) = -\rho_m g' h \left(u \frac{\partial B}{\partial x} + v \frac{\partial B}{\partial y}\right) \quad (5)$$

$$-\frac{1}{2}(u^2 + v^2) \sum_{i_s=1}^{n_s} (\rho_{s,i_s} D S_{s,i_s}) - \sum_{i_s=1}^{n_s} (\rho_{s,i_s} C_{s,i_s} T D S_{s,i_s}) + C_a \rho_a T_a E_a + C_{wv} \rho^b_{wv} {}_{wv,b} T_b E_{wv}.$$

where C_v is the mass averaged specific heat of the mixture, C_{s,i_s}, C_a and C_{wv} are the specific heat of solid, air and water vapour, respectively, and T_a and T_b are the atmospheric air and water vapour temperatures before entrainment. In this equation, heat transfer by thermal conduction is neglected, as well as thermal radiation. The full derivation of the energy equation is presented in Appendix A2.

It is worth noting that the design of conservative and stable numerical schemes for the solution of Eqs. (2-5) requires some care. This is because the numerical solution of mass and momentum equations, even when these quantities are globally conserved, does not necessarily result in an accurate description of the mechanical energy balance of the shallow water system

(Fjordholm et al., 2011; Murillo and García-Navarro, 2013). ~~This can lead to numerical~~ In fact, many numerical schemes perform well in practice but they may have an excessive amount of numerical dissipation near shocks, preventing a correct energy dissipation property across discontinuities (which can arise even in the case of smooth topography). A quantification of the error in the conservation of mechanical energy is beyond the scope of this paper, also because the error is case dependent and the topography plays a crucial role, but the reader can refer to Arakawa and Lamb (1977); Arakawa (1997); Arakawa and Lamb (1981); Fjo for a comprehensive discussion of this issue. In general, to guarantee energy conservation in smooth regimes, it is desirable to design high-order schemes adding a minimal amount of numerical dissipation.

Numerical errors in the computation of the mechanical energy may also lead to errors associated with the mixture temperature obtained from the total mixture specific energy and the kinetic energy computed from mass and momentum equations. For this reason, in some cases, instead of the full energy equation as presented above, it is preferable to solve a simpler transport equation for the specific thermal energy $C_v T$:

$$\frac{\partial}{\partial t}\left(\rho_m h C_v T\right) + \frac{\partial}{\partial x}\left(C_v T \rho_m h u\right) + \frac{\partial}{\partial y}\left(C_v T \rho_m h v\right) = \tag{6}$$

$$-\sum_{i_s=1}^{n_s}\left(\rho_{s,i_s} C_{s,i_s} T \underline{D}\underline{S}_{s,i_s}\right) + C_a \rho_a T_a E_a + C_{wv} \underline{\rho^b_{wv}}\underline{wv,b} T_b E_{wv},$$

We remark that in this equation we neglect heating associated with friction forces. This term can be important for some applications where viscous forces are particularly large, for example lava flows, but are negligible for the applications presented in this work. It is also worth noting that the numerical solution of Eqs. (2-4,6) does not guarantee that the total energy is conserved. In the following of the section, for simplicity, we use the temperature equation to demonstrate the writing of the system of equations in a more compact form and in the description of the numerical schemes, but for the applications presented in this work the full energy equation is solved.

~~Additional~~ The amounts of solid particles and water vapour in the flow vary in space and time because of sedimentation and entrainment, respectively, and for this reason additional transport equations for the mass of n_s solid classes and the water vapour are also considered:

$$\frac{\partial \alpha_{s,i_s}\rho_{s,i_s} h}{\partial t} + \frac{\partial\left(\alpha_{s,i_s}\rho_{s,i_s} h u\right)}{\partial x} + \frac{\partial\left(\alpha_{s,i_s}\rho_{s,i_s} h v\right)}{\partial y} = -\rho_{s,i_s}\underline{D}\underline{S}_{s,i_s}, \quad i_s = 1,\ldots,n_s \tag{7}$$

$$\frac{\partial \alpha_{wv}\rho_{wv} h}{\partial t} + \frac{\partial\left(\alpha_{wv}\rho_{wv} h u\right)}{\partial x} + \frac{\partial\left(\alpha_{wv}\rho_{wv} h v\right)}{\partial y} = \underline{\rho^b_{wv}}\underline{wv,b} E_{wv}. \tag{8}$$

Introducing the vector of conservative variables

$$\mathbf{Q} = (Q_1, \ldots, Q_{5+n_s})^T = \begin{bmatrix} \rho_m h \\ \rho_m hu \\ \rho_m hv \\ \rho_m h C_v T \\ \rho_{s_1} \alpha_{s_1} h \\ \vdots \\ \rho_{s_n} \alpha_{s_n} h \\ \rho_{wv} \alpha_{wv} h \end{bmatrix}. \tag{9}$$

it is possible to write the transport equations in the compact form:

$$\mathbf{Q}_t + \mathbf{F}(\mathbf{Q})_x + \mathbf{G}(\mathbf{Q})_y = \mathbf{S}_1(\mathbf{Q}) + \mathbf{S}_2(\mathbf{Q}) + \mathbf{S}_3(\mathbf{Q}), \tag{10}$$

where the fluxes $\mathbf{F}$ and $\mathbf{Q}$ are

$$\mathbf{F}(\mathbf{Q}) = \begin{bmatrix} \rho_m hu \\ \rho_m hu^2 + \rho_m g' \frac{h^2}{2} \\ \rho_m huv \\ C_v T \rho_m hu \\ \alpha_{s,1} \rho_{s,1} hu \\ \vdots \\ \alpha_{s,n} \rho_{s,n} hu \\ \alpha_{wv} \rho_{wv} hu \end{bmatrix} \quad \mathbf{G}(\mathbf{Q}) = \begin{bmatrix} \rho_m hv \\ \rho_m huv \\ \rho_m hv^2 + \rho_m g' \frac{h^2}{2} \\ C_v \rho_m hv \\ \alpha_{s,1} \rho_{s,1} hv \\ \vdots \\ \alpha_{s,n} \rho_{s,n} hv \\ \alpha_{wv} \rho_{wv} hv \end{bmatrix}, \tag{11}$$

the source terms $\mathbf{S_1}$ and $\mathbf{S_2}$ associated with the topography/gravitational and friction forces are

$$\mathbf{S}_1(\mathbf{Q}) = \begin{bmatrix} 0 \\ -\rho_m g' h \frac{\partial B}{\partial x} \\ -\rho_m g' h \frac{\partial B}{\partial y} \\ 0 \\ 0 \\ \vdots \\ 0 \end{bmatrix}, \quad \mathbf{S}_2(\mathbf{Q}) = \begin{bmatrix} 0 \\ F_x \\ F_y \\ 0 \\ 0 \\ \vdots \\ 0 \end{bmatrix} \tag{12}$$

and the source term $\mathbf{S_3}$ associated with ~~deposition~~ sedimentation and entrainment is

$$\mathbf{S}_3(\mathbf{Q}) = \begin{bmatrix} -\sum_{i_s=1}^{n_s}[\rho_{s,i_s} S_{s,i_s}] + \rho_a E_a + \rho_{wv} E_{wv} \\ -u\sum_{i_s=1}^{n_s}(\rho_{s,i_s} S_{s,i_s}) \\ -v\sum_{i_s=1}^{n_s}(\rho_{s,i_s} S_{s,i_s}) \\ -\sum_{i_s=1}^{n_s}(\rho_{s,i_s} C_{s,i_s} T S_{s,i_s}) + C_a \rho_a T_a E_a \\ -\rho_{s,1} S_{s,1} \\ \vdots \\ -\rho_{s,n} S_{s,n} \\ \rho_{wv} E_{wv} \end{bmatrix}. \tag{13}$$

Finally, it is possible to use the following equation ~~describes~~ to describe the temporal evolution of the topography:

$$\frac{\partial B}{\partial t} = \sum_{i_s=1}^{n_s} DS_{s,i_s}. \tag{14}$$

This equation assumes that sedimentation of particles immediately results in an increase in deposit thickness, which is not always the case, because particles in the basal layer that forms at the bottom of the flow could be moved as a traction carpet or even re-entrained. For the applications to dilute PDCs presented in this work, Eq. (14) is not used, while it is appropriate for other flows that can be modeled by the system of conservation equations (10), as for example for lahars or more concentrated PDCs.

The model described by the equations above generalize that presented by de' Michieli Vitturi et al. (2019) for granular flows, where the mixture was treated as a single-phase granular fluid. In fact, by neglecting ~~deposition~~ sedimentation and entrainment terms and the transport equation for water-vapour, the gas-particle mixture behaves as a homogeneous phase with constant density and temperature. In addition, if we use the Voellmy-Salm friction rheology, the system of equations becomes equivalent to that presented in de' Michieli Vitturi et al. (2019). This rheological model is available in IMEX_Sflow2D v2, together with a plastic rheology (Kelfoun, 2011), a temperature dependent friction model (Costa and Macedonio, 2005) and a lahar rehology (O'Brien et al., 1993), largely increasing the range of applicability of this version of the code.

It is important to remark that here, in comparison to Shimizu et al. (2017b, 2019), we do not enforce a front condition for the propagating flow, in terms of front velocity or ~~Freude~~ Froude number. As described in Marino et al. (2005), this condition applies to channelized flows for a phase during which, after an initial acceleration (as for lock-exchange experiments), the velocity of the front becomes constant (then followed by a front deceleration). The code we present is mostly aimed at simulating 1D/2D ~~spreading~~ flows, for which we do not simulate the initial phase and, most importantly, for which in radially spreading flows the front velocity decreases because of the ~~radial spread~~increasing radius. An alternative approach, which allows a correct simulation of the behavior of shocks without additional closure relations for the front, has been proposed in Fyhn et al. (2019). This approach relies on a formulation of the momentum equation in a non-conservative form, but at present is applicable for 1D shallow water equations only, and further studies are needed to adapt it to the 2D formulation. The application of modified finite-volume central-upwind schemes for non-conservative terms, as those proposed in Diaz et al.

(2019), could provide a reliable framework for the implementation in IMEX-SfloW2D of the approach described in Fyhn et al. (2019), in order to better simulate the constant velocity phase of channelized flows.

3 Constitutive equations for dilute turbulent currents

The system of conservation equations described by Eq. (10) represents the set of partial differential equations governing the transient dynamics of the multiphase flow of interest, but their physical and mathematical description is not complete without some closure relations describing the properties of the flow (density, ~~deposition~~sedimentation, entrainment, friction) as functions of the conservative or primitive variables. These relations are called constitutive equations, and they characterize the different flows we can solve with the model. In particular, in this section we describe the constitutive equations used to model dilute turbulent gas-particle currents. It is important to remark that, with appropriate choice of the friction terms and the constitutive equations, the model can be applied to a wider range of geophysical flows such as pyroclastic avalanches or lahars.

3.1 Gas density

Density of air and water vapour are computed using the ideal gas law, expressed as a function of temperature and pressure:

$$\rho_a = \frac{P}{R_{sp,a}T}, \qquad \rho_{wv} = \frac{P}{R_{sp,wv}T}. \tag{15}$$

Here, P is the ambient pressure (Pa) and $R_{sp,a}$ and $R_{sp,wv}$ are the specific gas constant for dry air and water vapour, respectively. The specific gas constants are provided in the code as user inputs, and more gas can be added, allowing for the simulation of a mixture of any number of gas components. We remark that we assume that density does not change with changes in hydrostatic pressure within the flow, but only with changes in flow temperature (Bursik and Woods, 1996; Shimizu et al., 2019).

3.2 Mixture density

Mixture density has already been introduced in Section 2 and it is given by Eq. ~~1~~(1).

3.3 Air entrainment

In large scale natural flows, entrainment of ambient fluid into a gravity current can be significant, diluting the flow to the point where it can becomes buoyant. As the flow propagates, air is entrained at a rate which: (i) is proportional to the magnitude of the difference in velocity between the flow and the stationary ambient; and (ii) depends on the ratio of the stabilizing stratification of the current ($N^2 = \frac{g}{\rho}\frac{\Delta\rho}{\Delta z}$, where N is the Brunt-Väisälä frequency) to destabilizing velocity shear ($M^2 = \left(\frac{\Delta u}{\Delta z}\right)^{-2}$, where M is also called the the Prandtl frequency). This ratio is expressed by the Richardson number ~~$Ri = g'h/(u^2 + v^2)$~~, (Cushman-Roisin and Beckers, 2011; Chow, 1959) and, following Bursik and Woods (1996), it is written here in the following equivalent form:

$$Ri = g'h/(u^2 + v^2) = (g\Delta\rho)/[\rho_m(u^2 + v^2)],$$

where g' is the reduced gravity. ~~Thus, following~~ Written in this form, this is essentially a ratio between between potential and kinetic energies, with the numerator being the potential energy needed to entrain the overlying buoyant fluid and the denominator being the kinetic energy of the flow which cause this entrainment.

Thus, according to Morton et al. (1956), we take the volumetric rate of entrainment of ambient air into the flow due to turbulent mixing as:

$$E_a = \epsilon\sqrt{(u^2+v^2)} \tag{16}$$

where ϵ ~~is the entertainment~~ , following Bursik and Woods (1996), is the entrainment coefficient given by Parker et al. (1987):

$$\epsilon = \frac{0.075}{(1+718Ri^{2.4})^{0.5}}. \tag{17}$$

We remark that, even if not implemented in the model, there are other relationships available in the literature for the entrainment coefficient (Ancey, 2004; Dellino et al., 2019a).

The Richardson number is important not only for the entrainment of ambient air, but also because the value $Ri = 1$ represents a critical threshold between subcritical ($Ri > 1$) and supercritical ($Ri < 1$) regimes, i.e. between a regime where flow velocity is slower than the speed with which gravity waves propagate (wave celerity) and a velocity where flow velocity is faster than wave celerity. Thus, the Richardson number is important also when boundary conditions are prescribed. We remark that at an inlet it is not possible to prescribe all the flow variables for subcritical flows, because the dynamics are also controlled by downstream conditions.

3.4 Water vapour entrainment

The entrainment of water vapour resulting from the interaction of the flows with water is modeled following the ideas presented in Dufek et al. (2007). A series of experiments have shown that the amount of heat transfer is governed by the rate of particle ~~deposition~~ sedimentation onto the water surface. At the water surface, steam is produced around the particles and ingested into the flow, but as particles sink deeper into the water, the steam produced condenses and is no longer available to be ingested into the flow. Thus, only a fraction of the thermal energy lost by the particles deposited by the flow over water contributes to the "effective" steam production. The coefficients $\gamma_{i_s,wv}$ represent the fraction of thermal energy from the particles of class i_s lost by the flow which results in the production of water vapour entrained in the flow. Thus, it is null when the current travels over land and between 0 and 1 when the current travels over water. As shown in (Dufek et al., 2007), as a first order approximation, 10% of the thermal energy of the particles is partitioned and is available to produce steam ($\gamma_{i_s,wv} = 0.1$), and smaller particles have greater steam production rates ($\gamma_{i_s,wv} > 0.1$).

The rate of water vapour production associated with this process is obtained with a balance of the rate of thermal energy lost by the particles and that necessary to produce the steam:

$$\rho^b_{wv} w_{v,b} E_{wv} \left[C_l(T_b - T_l) + L_w\right] = \sum_{i_s=1}^{n_s} \gamma_{i_s,wv}(\rho_{s,i_s} C_{s,i_s} T D S_{s,i_s}) \tag{18}$$

where ~~ρ_{wv}^{b}~~ $\rho_{wv,b}$ is the density of water vapour at boiling point, C_l is the specific heat of liquid water, T_l is the temperature of water, T_b is the boiling temperature, and L_w is the latent heat of vaporization.

3.5 Sedimentation

Sedimentation of particles from the flow is modeled as a mass flux at the flow bottom and is assumed to occur at a rate which is proportional to the particle settling velocity v_s, to the bulk density of particles in the flow and to a factor depending on the total solid volume fraction (Bürger and Wendland, 2001), accounting for hindered settling phenomena:

$$DS_s = \alpha_s \cdot v_s(d_s) \left(1 - \frac{\sum \alpha_s}{\alpha_{max}}\right)^n \qquad n > 1 \tag{19}$$

where α_{max} is the maximum volume fraction of solids, which generally occurs at fractions between 0.6 and 0.7, while n is an empirical exponent (4.65 is a suitable value for rigid spheres).

The particle settling velocity v_s is a function of the particle diameter d_s, and is given by the following non-linear equation:

$$v_s^2(d_s) C_D(\mathrm{Re}) = \frac{4}{3} d_s g \left(\frac{\rho_s - \rho_a}{\rho_a}\right). \tag{20}$$

~~The~~ In the actual version of the code, the gas-particle drag coefficient $C_D(\mathrm{Re})$ is given by the following relations, as a function of the Reynolds number $\mathrm{Re} = \frac{d_s v_s}{\nu}$ (Lun and Gidaspow, 1994):

$$\begin{aligned} \mathrm{Re} > 1000; \qquad C_D(\mathrm{Re}) &= 0.44 \\ \mathrm{Re} \leq 1000; \qquad C_D(\mathrm{Re}) &= \frac{24}{\mathrm{Re}} \left(1 + 0.15 \mathrm{Re}^{0.687}\right) \end{aligned}$$

and ν is the kinematic viscosity coefficient of atmospheric air.

Eq. ~~20~~ (20) has an analytical solution in the limit of coarse particles ($Re > 1000$), :

$$v_s(d_s) = \sqrt{\frac{4}{3 C_D} \left(\frac{\rho_s - \rho_a}{\rho_a}\right) d_s g}, \tag{21}$$

and in the limit of very fine particles ($Re << 1$):

$$v_s(d_s) = \frac{d_s^2}{18\nu} \left(\frac{\rho_s - \rho_a}{\rho_a}\right) g. \tag{22}$$

In the intermediate regimes, Eq. ~~20~~ (20) is solved numerically.

The sedimentation model described by Eq. (19) represents the loss of particles from the flow, but does not necessarily correspond to a deposition rate, i.e. the rate of accretion of deposit thickness. This is true only when the ratio between the actual deposition and the sedimentation rate is high ($\gtrsim 5 \times 10^{-3}$ according to Shimizu et al., 2019) In fact, there may be processes at the deposition interface that mobilize or even re-entrain the particles settling into the basal layer and then onto the ground. Furthermore, in order not to add further complexity, the adopted equation assumes a sedimentation rate which does not take into account the turbulence, which can keep the particles in suspension. A more comprehensive description of sedimentation based on the Rouse number, representing a ratio of particle settling velocity to scale of turbulence, can be found in (Dellino et al., 2019b, 2020; Valentine, 1987).

3.6 Friction model

Several friction models have been implemented in the numerical code. For the applications presented in this work, a simple model has been used, with the force being proportional to the square of flow velocity through a basal friction coefficient f depending on terrain roughness:

$$\mathbf{F} = (F_x, F_y) = -f\rho_m\sqrt{(u^2+v^2)}(u,v). \tag{23}$$

The friction factor typically has a value in the range 0.001-0.02 (Bursik and Woods, 1996). This form is equivalent to the Voellmy-Salm model (Bartelt et al., 1999) when the contribution of the basal Coulomb friction is neglected.

4 Numerical discretization

In this section we present the details of the numerical scheme implemented to solve the system of equations (10). It is important to remark that different processes contributing to the dynamics of the flows of interest have different time scales, and thus they require different numerical techniques. For this reason, a splitting approach is adopted in the code to integrate separately: (i) the advective, gravitational and frictional terms; and (ii) the ~~deposition~~ sedimentation and entrainment terms.

The numerical solver for the solution of Eq. (10) (without the ~~deposition~~ sedimentation and entrainment terms represented by $\mathbf{S}_3$) is based, as in de' Michieli Vitturi et al. (2019), on an IMEX Runge-Kutta scheme, where the conservative fluxes $\mathbf{F}$ and $\mathbf{G}$ and the terms $\mathbf{S}_1$ are treated explicitly, while the stiff terms of the equations, represented by $\mathbf{S}_2$, are discretized implicitly (Pareschi and Russo, 2005). The use of an implicit scheme for friction terms allows for larger time steps and to properly model conditions such as initiation and cessation phases, without the need for empirical thresholds on the velocity or thickness of the flow. For the spatial discretization of the fluxes, as in the first version of the code, we adopt a central-upwind finite-volume method (Kurganov et al., 2001; Kurganov and Petrova, 2007; de' Michieli Vitturi et al., 2019; Biagioli et al., 2021) on co-located grids derived from DEMs in UTM coordinates, thus on uniform grids of equally sized square pixels. The central-upwind approach guarantees an accurate description of the propagation of the dry/wet interface (front of the flow) and the positivity of the solution.

We denote the vector of discretized values of the conservative variables with $\mathbf{Q}_{j,k}$, where the first index refers to the longitude and the second to the latitude. These values represent the average value of the conservative variables on each computational cell and are associated to the cell centers (see Figure 1). Similarly, the discretized values of the topography elevation $\mathbf{B}_{j,k}$ are saved at the cell centers. We also use the superscripts E, W, N, and S to denote the east, west, north and south values of the variables inside a cell. Discontinuities are allowed for in the numerical solution at the cell interfaces. In fact, at the interface $(j+\frac{1}{2},k)$ we can have two distinct values of the numerical solutions, $\mathbf{Q}^E_{j,k}$ and $\mathbf{Q}^W_{j+1,k}$ (see Figure 1). This is true also for the discretized topography. From the set of conservative variables $\mathbf{Q}$, a second set of variables, which we will call *primitive variables*, is derived:

$$\mathbf{P} = (h, hu, hv, T, h\alpha_{s,1}, \ldots, h\alpha_{s,n_s}, h\alpha_{wv}, u, v) \tag{24}$$

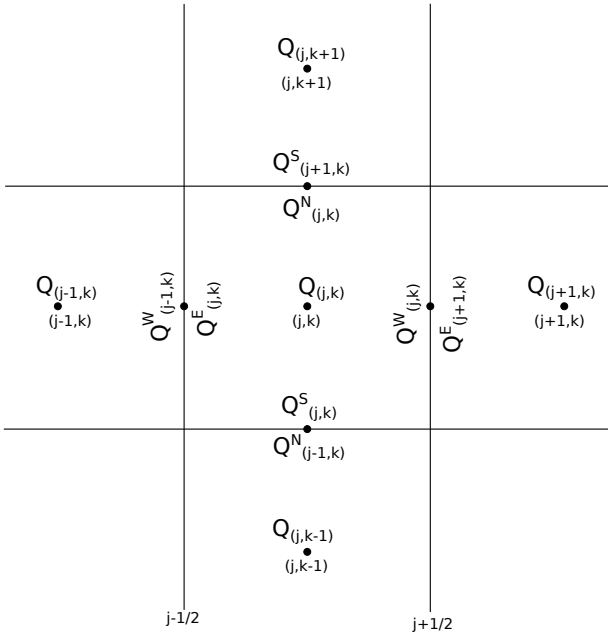

Figure 1. Sketch of the numerical grid and conservative variables indexing. The average value of the vector of conservative variables on each computational cell is denoted by $\mathbf{Q}_{j,k}$ and is associated to the cell center. The vectors $\mathbf{Q}^E_{j,k}$, $\mathbf{Q}^W_{j,k}$, $\mathbf{Q}^N_{j,k}$ and $\mathbf{Q}^S_{j,k}$ are defined at the cell interfaces and represents the interface values of the conservative variables. At each interface two interface vectors are defined.

The full derivation of the primitive variables from the conservative variables is presented in the Appendix. We remark that, following Kurganov and Petrova (2007), when the velocities u and v are computed from the conservative variables $Q_2 = \rho_m hu$ and $Q_3 = \rho_m hv$, a desingularization is applied to avoid large velocities that might arise because of the division by very small values of thickness, as it could occur close to the flow front.

From the values of the primitive variables $\mathbf{P}_{j,k}$ at the cell centers, the partial derivatives $(\mathbf{P}_x)_{j,k}$ and $(\mathbf{P}_y)_{j,k}$ are computed, using opportune slope limiters (MinMod, Superbee or Van Leer). ~~Then~~Slope limiters are employed to mitigate the occurrence of excessive oscillations and unrealistic behavior that might arise during the solution of partial differential equations through finite volume methods, especially in proximity to shocks and discontinuities. When prioritizing accurate shock representation, the Superbee slope limiter can be the best choice as it maintains sharper discontinuities, but at the cost of a tendency of smooth humps to become steeper and squared with time. If preserving monotonicity and minimizing oscillations in smooth regions are more important, then MinMod could be favored. For a more detailed analysis of slope limiters and finite volume methods, the reader can refer to LeVeque (2002). Once the partial derivatives are computed, the values at the internal sides of each cell interface are reconstructed with a linear interpolation from the cell center values:

$$\mathbf{P}^E_{j,k} = \mathbf{P}_{j,k} + \frac{\Delta x}{2}(\mathbf{P}_x)_{j,k}, \qquad \mathbf{P}^W_{j,k} = \mathbf{P}_{j,k} - \frac{\Delta x}{2}(\mathbf{P}_x)_{j,k},$$
$$\mathbf{P}^N_{j,k} = \mathbf{P}_{j,k} + \frac{\Delta y}{2}(\mathbf{P}_y)_{j,k}, \qquad \mathbf{P}^S_{j,k} = \mathbf{P}_{j,k} - \frac{\Delta y}{2}(\mathbf{P}_y)_{j,k}.$$

This choice for primitive variables allows prescription of the boundary conditions at the cell interfaces in a natural way, because usually they are given in terms of flow thickness, volumetric flow rate, phases fractions and temperature, or in terms of their gradient. Having two different values at the two sides of interfaces in a numerical method might seem counterintuitive from a physical standpoint. However, these jumps are a consequence of the mathematical discretization process used in the finite volume method to approximate continuous partial differential equations over discrete domains. In particular, having two values at the two sides of interfaces in finite volume methods is essential for properly describing and capturing discontinuous solutions (LeVeque, 2002).

Once the primitive variables at the interfaces are known (either from the reconstruction or from the boundary conditions at the boundary cells), we compute the corresponding conservative variables $\mathbf{Q}^E_{j,k}$, $\mathbf{Q}^W_{j,k}$, $\mathbf{Q}^N_{j,k}$ and $\mathbf{Q}^S_{j,k}$. Primitive and conservative variables are then used to compute the fluxes $\mathbf{F}(\mathbf{P}^{(\cdot)}_{j,k}, \mathbf{Q}^{(\cdot)}_{j,k})$ and $\mathbf{G}(\mathbf{P}^{(\cdot)}_{j,k}, \mathbf{Q}^{(\cdot)}_{j,k})$ at the sides of the interfaces. We observe that the set of primitive variables is redundant, but this redundancy allows us to obtain a stable numerical scheme. In particular, for the advective flux terms, the advection velocity components are obtained from the primitive variables, while the variables to advect are taken directly from the conservative variables. The use of this combination of reconstructed primitive and conservative variables for the calculation of the fluxes, together with the application of limiters, makes the numerical scheme stable, avoiding the origin of large values of thickness and velocity. The fluxes at the two sides of each interface are then used to compute the numerical fluxes.

Following Kurganov and Petrova (2007), the numerical fluxes in the x-direction are given by:

$$\mathbf{H}^x_{j+\frac{1}{2},k} = \frac{a^+_{j+\frac{1}{2},k}\mathbf{F}(\mathbf{P}^E_{j,k}, \mathbf{Q}^E_{j,k}) - a^-_{j+\frac{1}{2},k}\mathbf{F}(\mathbf{P}^W_{j+1,k}, \mathbf{Q}^W_{j+1,k})}{a^+_{j+\frac{1}{2},k} - a^-_{j+\frac{1}{2},k}} + \frac{a^+_{j+\frac{1}{2},k}a^-_{j+\frac{1}{2},k}}{a^+_{j+\frac{1}{2},k} - a^-_{j+\frac{1}{2},k}}\left(\mathbf{Q}^W_{j+1,k} - \mathbf{Q}^E_{j,k}\right) \tag{25}$$

where the right- and left-going local speeds $a^+_{j+\frac{1}{2},k}$ and $a^-_{j+\frac{1}{2},k}$ are estimated by:

$$a^+_{j+\frac{1}{2},k} = \max\left(u^E_{j,k} + \sqrt{g' h^E_{j,k}}, u^W_{j+1,k} + \sqrt{g' h^W_{j+1,k}}, 0\right),$$
$$a^-_{j+\frac{1}{2},k} = \min\left(u^E_{j,k} - \sqrt{g' h^E_{j,k}}, u^W_{j+1,k} - \sqrt{g' h^W_{j+1,k}}, 0\right).$$

It is important here to remark that we have two local speeds not because they are associated to the two different sides of each interface, but because one is for the left-going characteristic speeds (on both sides) and the other for the right-going speeds (on both sides).

In a similar way, the numerical fluxes in the $y-$direction are given by:

$$\mathbf{H}^y_{j,k+\frac{1}{2}} = \frac{b^+_{j,k+\frac{1}{2}}\mathbf{G}(\mathbf{P}^N_{j,k}, \mathbf{Q}^N_{j,k})) - b^-_{j,k+\frac{1}{2}}\mathbf{G}(\mathbf{P}^S_{j+1,k}, \mathbf{Q}^S_{j+1,k})}{b^+_{j,k+\frac{1}{2}} - b^-_{j,k+\frac{1}{2}}} + \frac{b^+_{j,k+\frac{1}{2}}b^-_{j,k+\frac{1}{2}}}{b^+_{j,k+\frac{1}{2}} - b^-_{j,k+\frac{1}{2}}}\left(\mathbf{Q}^S_{j+1,k} - \mathbf{Q}^N_{j,k}\right) \tag{26}$$

where the local speeds in the $y-$direction $b^{+}_{j+\frac{1}{2},k}$ and $b^{-}_{j+\frac{1}{2},k}$ are given by:

$$b^{+}_{j,k+\frac{1}{2}} = \max\left(v^{N}_{j,k} + \sqrt{g' h^{N}_{j,k}}, v^{S}_{j,k+1} + \sqrt{g' h^{S}_{j,k+1}}, 0\right),$$
$$b^{-}_{j,k+\frac{1}{2}} = \min\left(v^{N}_{j,k} - \sqrt{g' h^{N}_{j,k}}, v^{S}_{j,k+1} - \sqrt{g' h^{S}_{j,k+1}}, 0\right).$$

The explicit computation of the term $\mathbf{S_1}$ requires the numerical discretization of the spatial gradient of the topography. The partial derivatives $(B_x)_{j,k}$ and $(B_y)_{j,k}$ are computed from the cell averages using the same slope limiter used for h. Then, the topography is computed at the interfaces with a linear reconstruction, obtaining for each cell the values:

$$\mathbf{B}^{E}_{j,k} = \mathbf{B}_{j,k} + \frac{\Delta x}{2}(\mathbf{B}_x)_{j,k}, \qquad \mathbf{B}^{W}_{j,k} = \mathbf{B}_{j,k} - \frac{\Delta x}{2}(\mathbf{B}_x)_{j,k},$$
$$\mathbf{B}^{N}_{j,k} = \mathbf{B}_{j,k} + \frac{\Delta y}{2}(\mathbf{B}_y)_{j,k}, \qquad \mathbf{B}^{S}_{j,k} = \mathbf{B}_{j,k} - \frac{\Delta y}{2}(\mathbf{B}_y)_{j,k}.$$

The implicit part of the IMEX Runge-Kutta scheme, associated with the integration of the friction terms, is solved using a Newton-Raphson method with an optimum step size control, where the Jacobian of the implicit terms is computed with ~~a~~ an automatic complex-step derivative approximation (de' Michieli Vitturi et al., 2019). The implicit treatment of the friction terms, when dealing with strongly nonlinear rheologies, avoids many problems related to the proper stopping condition of the flow, without the need for introducing arbitrary thresholds. In addition, the automatic derivation of the friction term allows for a simple implementation of additional rheological models, including formulations dependent on any model parameter.

After each Runge-Kutta procedure, the ~~deposition~~ sedimentation and air entrainment term are computed explicitly and the flow variables and the topography at the centers of the computational cells are updated.

For large time steps, the explicit treatment of solid ~~deposition~~ sedimentation could lead to negative solid volumetric fractions in the flow, and for this reason the effective ~~deposition rate $\overline{D}_{s,is}$~~ sedimentation rate $\overline{S}_{s,is}$ is limited at each integration step in order to prevent this occurrence:

$$\overline{S}_{s,i_s} = \min\left[D S_{s,i_s}, \Delta t \cdot (\alpha_{s,i_s} h)\right].$$

The use of an explicit integration scheme for the terms of the equations containing spatial derivatives, with respect to an implicit treatment, has the advantage that the solutions of the discretized equations in each cell are decoupled, without the need to solve for a large linear system. The same is true for the integration of the friction, ~~deposition~~ sedimentation and entrainment terms. This allowed implementation of a parallel strategy to advance in time the numerical solution of the discretized equations, requiring almost no communication or dependency between the processes. Thus, with a small effort, the Fortran implementation of the code has been updated by parallelizing all the loops over the computational cells with the Open MultiProcessor (OpenMP) programming model for shared-memory platforms.

The schemes implemented for the numerical discretization of the governing equations do not depend on the particular choice of the constitutive equation or on the friction force, thus they apply also when the model is used to solve for different volcanic mass flows.

5 Numerical benchmarks

In this section we present applications of the model to 1D and 2D problems. They ~~add~~ provide some of the fundamental elements for verification and validation of the numerical model (following the terminology proposed by Oberkampf and Trucano, 2002; Es , adding to numerical benchmarks and validation tests previously presented by ~~(de' Michieli Vitturi et al., 2019)~~de' Michieli Vitturi et al. (2 . The 1D benchmark tests are designed to demonstrate the capability of the numerical scheme to describe the interaction of the flow of obstacles in different regimes (subcritical, supercritical, transitional). Then, model results are compared with those presented in ~~(Engwell et al., 2016)~~ Engwell et al. (2016) for large ash flows, to compare the steady state produced by our 2D transient simulations with that obtained with a 1D axisymmetric steady-state model.

5.1 One dimensional subcritical and transcritical flows

When dealing with flows where velocity and mixture density can experience large changes, it is important to have a model which properly describes both subcritical ($Ri > 1$) and supercritical ($Ri < 1$) regimes and the transition between them. In the subcritical regime, flow is dominated by gravitational forces, with greater thickness and lower velocities; for supercritical flow it is the opposite, with thinner and faster flow dominated by inertial forces. In addition, it is fundamental to have a model that is able to describe accurately how the flow interacts with the topography under these different regimes. As shown in Woods et al. (1998) using both laboratory experiments and theoretical models, when a flow interacts with a topographic barrier such as a ridge, the flow thickness and velocity can change in different ways depending on the height of the ridge and the flow speed (Houghton and Kasahara, 1968). Under some circumstances, flows may be partially blocked and producing upstream propagating bores resulting in increased sedimentation upstream of the barrier. In other cases, the flow is able to overcome the ridge, but with a transition in flow regime, and thus in the sedimentation pattern.

Here, we present some numerical simulations reproducing literature benchmarks and showing the capability of the numerical code to properly model the subcritical and supercritical regimes, and the transition between them. Following Goutal (1997); Delestre et al. (2013); Michel-Dansac et al. (2016), we simulate a steady one-dimensional flow in a 25 m domain with a parabolic bump on the bottom, where the topography is given by

$$B(x) = \begin{cases} 0.2 - 0.05(x-10)^2 & 8 < x < 12 \\ 0 & elsewhere \end{cases} \tag{27}$$

For the test cases presented in this section no friction, mass entrainment and sedimentation are considered. The flow travels in the $x-$direction ($u > 0$ m/s, $v = 0$ m/s), with constant density (for simplicity $\rho = 1$ ~~kgm~~kg m^{-3}) and constant temperature (energy equation is not needed). ~~Furthermore, no friction, mass entrainment and deposition are considered for the test cases presented in this section.~~ With these assumptions, in the steady state regime, we can derive from Eqs. (2-3) the following

simpler governing equations:

$$\begin{cases} \dfrac{\partial (hu)}{\partial x} = 0 \\ \\ \dfrac{\partial}{\partial x}\left(hu^2 + \dfrac{1}{2} g' h^2 \right) = -g' h \dfrac{\partial B}{\partial x} \end{cases} \tag{28}$$

By expanding the derivative on the left-hand side of the momentum equation, we obtain:

$$u \frac{\partial u}{\partial x} + g' \frac{\partial h}{\partial x} = -g' \frac{\partial B}{\partial x} \tag{29}$$

and, by substituting the expression of $\partial u / \partial x$ computed from the mass equation, we have

$$\left(1 - \frac{u^2}{g' h} \right) \frac{\partial h}{\partial x} = -\frac{\partial B}{\partial x} \tag{30}$$

which, written in terms of the Richardson number Ri, gives

$$\left(1 - \frac{1}{Ri} \right) \frac{\partial h}{\partial x} = -\frac{\partial B}{\partial x} \qquad or \qquad (1 - Ri) \frac{\partial}{\partial x}(h + B) = \frac{\partial B}{\partial x}. \tag{31}$$

According to these equations, the subcritical or supercritical regime determines whether flow thickness h and free surface $h + B$ increases or decreases as the fluid interacts with the topography. It is also important to observe that in supercritical flows ($Ri < 1$), upstream conditions fully determine the flow immediately downstream, while in subcritical flows changes in downstream conditions affect the flow upstream. From a numerical point of view, this is important when prescribing flow boundary conditions, because we can only prescribe all flow variables at the inlet for supercritical flows. We remark here that the test cases presented in this section are not meant to be representative of real dilute PDCs conditions, but they have been chosen to show the capability of the numerical model to properly simulate different flow regimes and their transitions.

By integrating Eq. (30) with the additional condition of constant volumetric flux, as epxressed by the first of Eqs. (28), we also have, in the case of a regular solution, the following Bernoulli equation:

$$\frac{(hu)^2}{2g'h^2} + h + z = Const, \tag{32}$$

which gives a relation between the topography elevation and the flow height. Using Eq. (32), in the cases of supercritical or subcritical flows without regime transitions, it is possible to obtain the following implicit equation for the flow depth (Delestre et al., 2013):

$$h(x)^3 + \left(B(x) - \frac{(h_0 u_0)^2}{2g' h_0^2} \right) h(x)^2 + \frac{(h_0 u_0)^2}{2g'} = 0, \tag{33}$$

where h_0 and u_0 are the flow thickness and velocity at the inlet or outlet of the domain, respectively.

The first test case is a flow where at the left boundary of the domain an influx with $h = 1$ m and $u = 10$ m s^{-1} is prescribed, resulting in a supercritical regime ($Ri < 10^{-2}$). As previously stated, the supercritical conditions at the inlet are consistent with

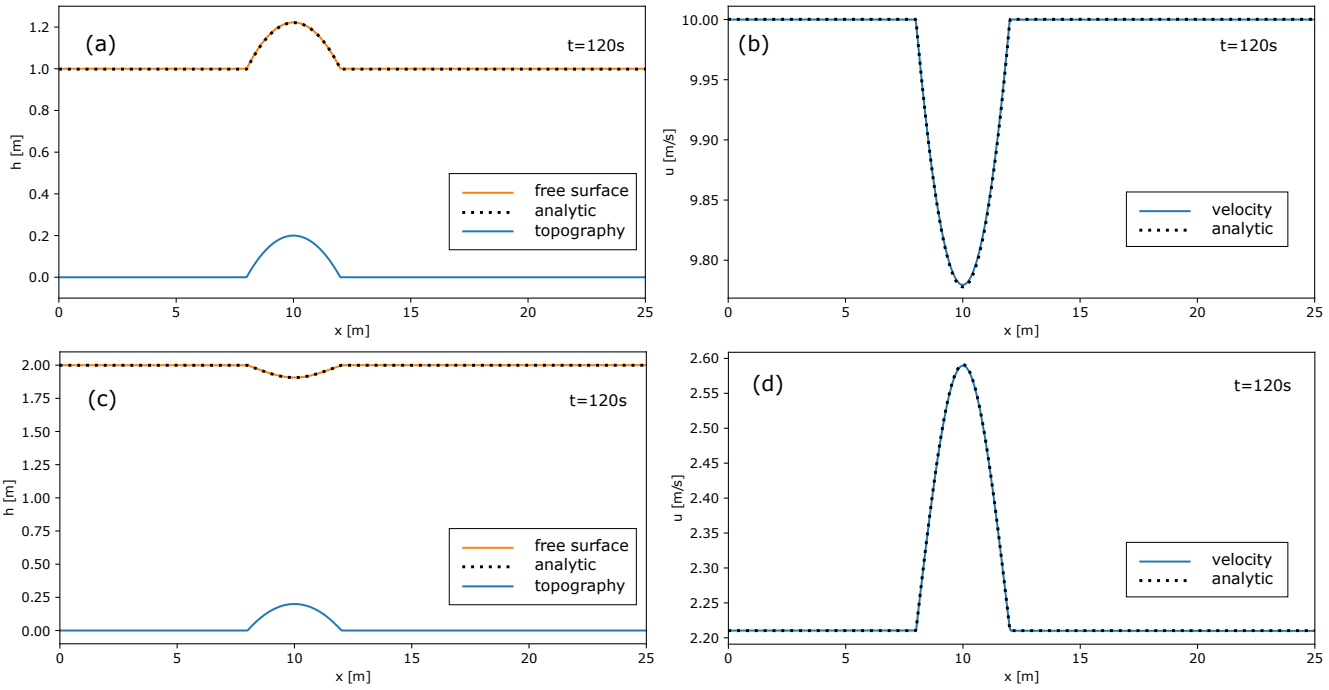

Figure 2. Thickness (left) and velocity (right) profiles in one-dimensional flows over a bump. Steady numerical solutions for supercritical and subcritical flows are shown with solid lines in top and bottom panels, respectively. The black dotted lines in each panel represent the analytical solutions, computed by solving Eq. (33).

the two boundary conditions assigned. For this simulation, as for the other simulations presented in this section, the domain is partitioned with 1000 uniform cells, and a linear reconstruction of the primitive variables with a minmod limiter has been used. For this supercritical test, the solution at $t = 0$ is initialized with a constant thickness corresponding to the inlet value and with zero velocity. The solution at $t = 120$ s, when a steady state is reached, is presented in terms of the flow free surface (Fig. 2a, orange line) and flow velocity (Fig. 2b). In this supercritical condition, the fluid thickens and slows as it passes over the top of the obstacle, reaching its minimum speed at the crest ($x = 10$ m). The slope of the free surface follows the slope of the obstacle, increasing before the crest and then decreasing in elevation. The higher the Richardson number, the smaller the effect of topography on flow thickness and on velocity, with the free surface mimicking the slope of the topography.

The second test case is a simulation of a subcritical regime. In this case an influx of 4.42 m^2 s^{-1} is prescribed at the left boundary, while a flow thickness of 2 m is fixed at the outlet. It is important to observe that here, in contrast to the previous case, we cannot prescribe both flow thickness and velocity at the inlet, because of the subcritical condition. Also for this case, the solution in the domain is initialized at $t = 0$ s with a constant thickness corresponding to the outlet value and with zero velocity. The numerical solution at $t = 120$ s, corresponding to a steady state, is presented in the bottom panel of Fig. 2. In this case, the fluid thins and accelerates as it crosses the top of the obstacle, reaching its maximum speed and minimum thickness at

the crest. Accordingly with the second of Eqs. (31), the free surface also decreases where the bottom slope is positive, while it increases after reaching the bottom crest. For both the first two test cases, we also computed the analytical solutions by means of the Bernoulli Equation (33) and the values are plotted with black dotted lines in Figure 2, showing a good correspondence with the numerical solutions (solid lines).

The interaction of a flow with an obstacle can also lead to a steady solution, with a transition in the flow regime (transcritical flow). The steady state conditions investigated here for these transonic (with and without shock) test cases are similar to that obtained in laboratory experiments presented in Fig. 4a of Woods et al. (1998), which showed that the deposit is weakly affected by the presence of the ridge and the regime transition. If the flow is subcritical upstream and it undergoes a sufficient increase in velocity and decrease in thickness as it ascends toward the crest, a smooth transition from subcritical to supercritical flow can occur. This transition is shown in the top panels of Fig. 3, representing the flow free surface at $t = 120$ s for a flow with an influx of 1.53 m^2 s^{-1} prescribed at the left boundary and a thickness of 0.66 m fixed at the outlet, when the flow is subcritical. In fact, when the flow becomes supercritical, no boundary condition can be prescribed at the outlet, and the outlet thickness is an outcome of the simulation (here $h = 0.4$ m). For this simulation, the solution in the domain is initialized at $t = 0$s with a constant free surface corresponding to the outlet subcritical value and with zero velocity. Also in the case of transcritical flow without shock it is possible to express, from the Bernoulli Eq. (32), the water height as the solution of a cubic equation (Delestre et al., 2013):

$$h(x)^3 + \left(B(x) - \frac{(h_0 u_0)^2}{2g' h_C^2} - h_C - B_M \right) h(x)^2 + \frac{(h_0 u_0)^2}{2g'} = 0, \tag{34}$$

where h_0 and u_0 are the flow thickness and velocity at the inlet or outlet of the domain, respectively, B_M is the maximum topography elevation, and h_C is the corresponding flow thickness, which can be computed analytically as (Delestre, 2010):

$$h_C = \left(\frac{h_0 u_0}{\sqrt{g'}} \right)^{2/3}.$$

The analytical solution of the Eq. (34) is reported in the top panels of Fig. 3 with a black dotted line.

Under certain conditions the flow, after an initial thinning and acceleration over the obstacle, can suddenly thicken and decelerate ~~in correspondence with~~ with a shock in correspondence of a flow regime transition. This transition from a rapid, supercritical flow to a slow, subcritical flow, called a hydraulic jump, is shown in Fig. 3, bottom panel, representing the flow free surface at $t = 120$ s for a flow with an influx of 0.18 m^2 s^{-1} prescribed at the left boundary and a thickness of 0.33 m fixed at the outlet. ~~The steady state conditions obtained for these transonic (with and without shock) test cases are similar to that obtained in laboratory experiments presented in Fig. 4a of Woods et al. (1998), which showed that the deposit is weakly affected by the presence of the ridge and the regime transition~~Following Delestre et al. (2013), flow thickness for the transcritical flow with

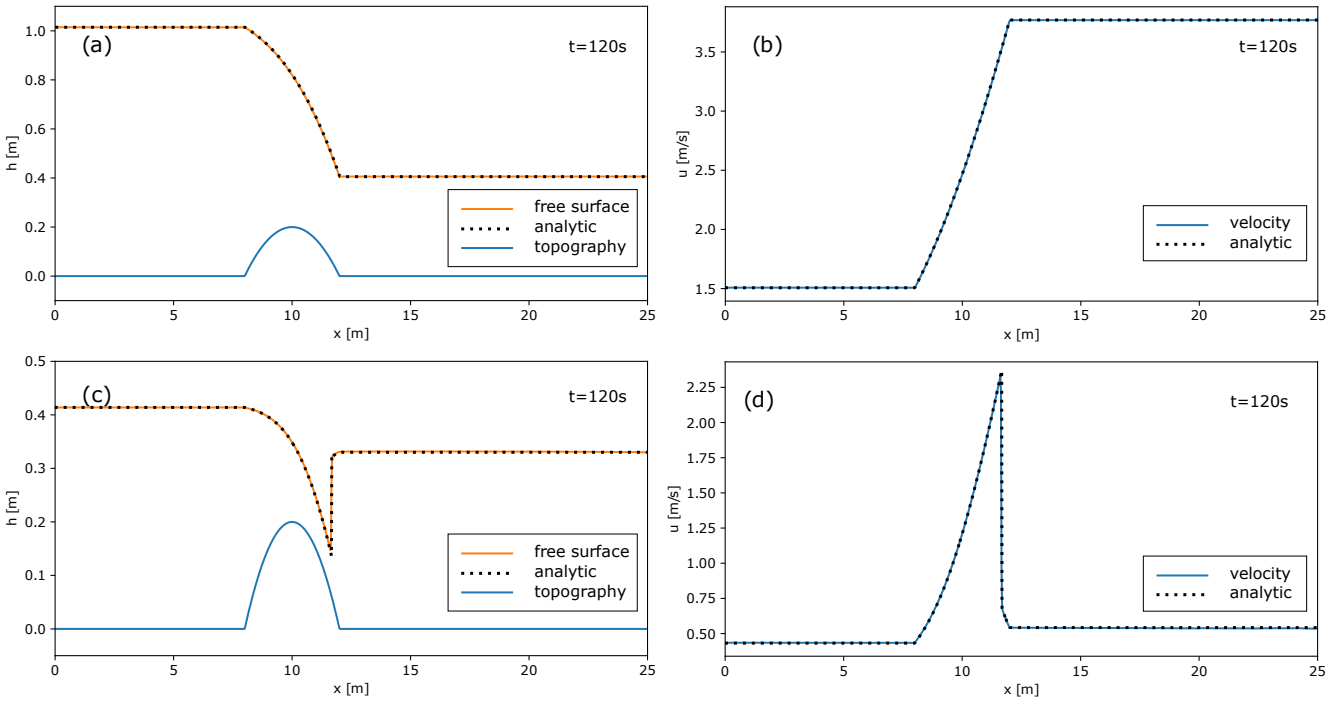

Figure 3. Flow thickness (left) and velocity (right) profiles in one-dimensional flows over a bump. Steady numerical solutions for transcritical flows without and with shock are shown with solid lines in top and bottom panels, respectively. The black dotted lines in each panel represent the analytical solutions, computed by solving Eqs. (34) and (35).

shock is given by the solution of

$$\begin{cases} h(x)^3 + \left(B(x) - \frac{(h_0 u_0)^2}{2g' h_C^2} - h_C - B_M\right) h(x)^2 + \frac{(h_0 u_0)^2}{2g'} = 0 & x < x_{shock} \\ h(x)^3 + \left(B(x) - \frac{(h_0 u_0)^2}{2g' h_0^2}\right) h(x)^2 + \frac{(h_0 u_0)^2}{2g'} = 0 & x > x_{shock} \\ (h(x)u(z))^2 \left(\frac{1}{h_1} - \frac{1}{h_2}\right) + \frac{g'}{2}(h_1^2 - h_2^2) = 0 \end{cases} \tag{35}$$

where B_M is the maximum topography elevation, h_0 and u_0 are the flow thickness and velocity at the outlet of the domain, respectively, h_C is the corresponding flow thickness, and h_1 and h_2 are the flow thicknesses upstream and downstream of the shock, respectively. The location of the shock x_{shock} is found from the last equation in Eq. (35), which is the Rankine-Hugoniot's condition (LeVeque, 2002). The analytical solution of the Eq. (35) is plotted in the bottom panels of Fig. 3 with a black dotted line, showing the accuracy of the numerical solver in the prediction of the shock location and amplitude for both flow thickness and velocity.

In addition to the literature test-cases described above, aimed at reproducing steady-state flows for different regimes, we present here another test case showing the temporal evolution of a flow with a steady inlet condition, where the interaction with an obstacle results in the transition from subcritical to supercritical regime, and the backward propagation of a hydraulic jump. The boundary conditions (inlet and outlet) are based on the configurations described in Khezri (2014) and Putra et al. (2019) and, as for the previous tests, we assume a constant density ($\rho = 1$ kg m^{-3}) and neglect friction, mass entrainment and ~~deposition~~sedimentation. The computational domain is 10 m long (discretized with 1000 cells) and the inlet flow velocity and thickness are fixed to 0.74 m s^{-1} and 0.14 m, respectively. The same values are used for the initial conditions up to 8 m from the inlet, while no flow is present beyond this distance. At a distance of 9m from the inlet, a 0.1 m high wall is present, represented by a discontinuity in the topography:

$$B(x) = \begin{cases} 0 & x \leq 9\ m, \\ 0.1 & x > 9\ m \end{cases}. \tag{36}$$

For this test case, no analytical solutions are available. Some snapshots of the first 40 s of the simulation are shown in 4, with the flow thickness on the left panels and the velocity on the right panels. When the flow front reaches the wall, flow thickness increases and its velocity decreases, with a transition from supercritical to subcritical regime. The transition zone propagates backward, similarly to a tidal bore. At the same time, due to an increase in flow thickness, part of the flow overcomes the obstacle and propagates beyond it. This behavior is similar to that illustrated in Woods et al. (1998), Fig. 9, for a large ash flow interacting with a ridge. While they interpreted the bore as a reflected part of the flow, which can carry fine-grained material back upstream, the right panels of Fig. 4 show that flow velocity is always positive. This means that, for the simulation presented here, the increase in flow thickness propagating upstream is not due to a negative flow velocity or a flow reflection, but to the backward propagation of the hydraulic jump. At later stages (not shown here) a steady state is reached, with the flow being subcritical before and supercritical after the wall. A similar behaviour can be expected when a supercritical PDC reaches a sufficiently high topographic obstacle. This, because of the transition to a subcritical regime, would result in an increased sedimentation rate before the obstacle.

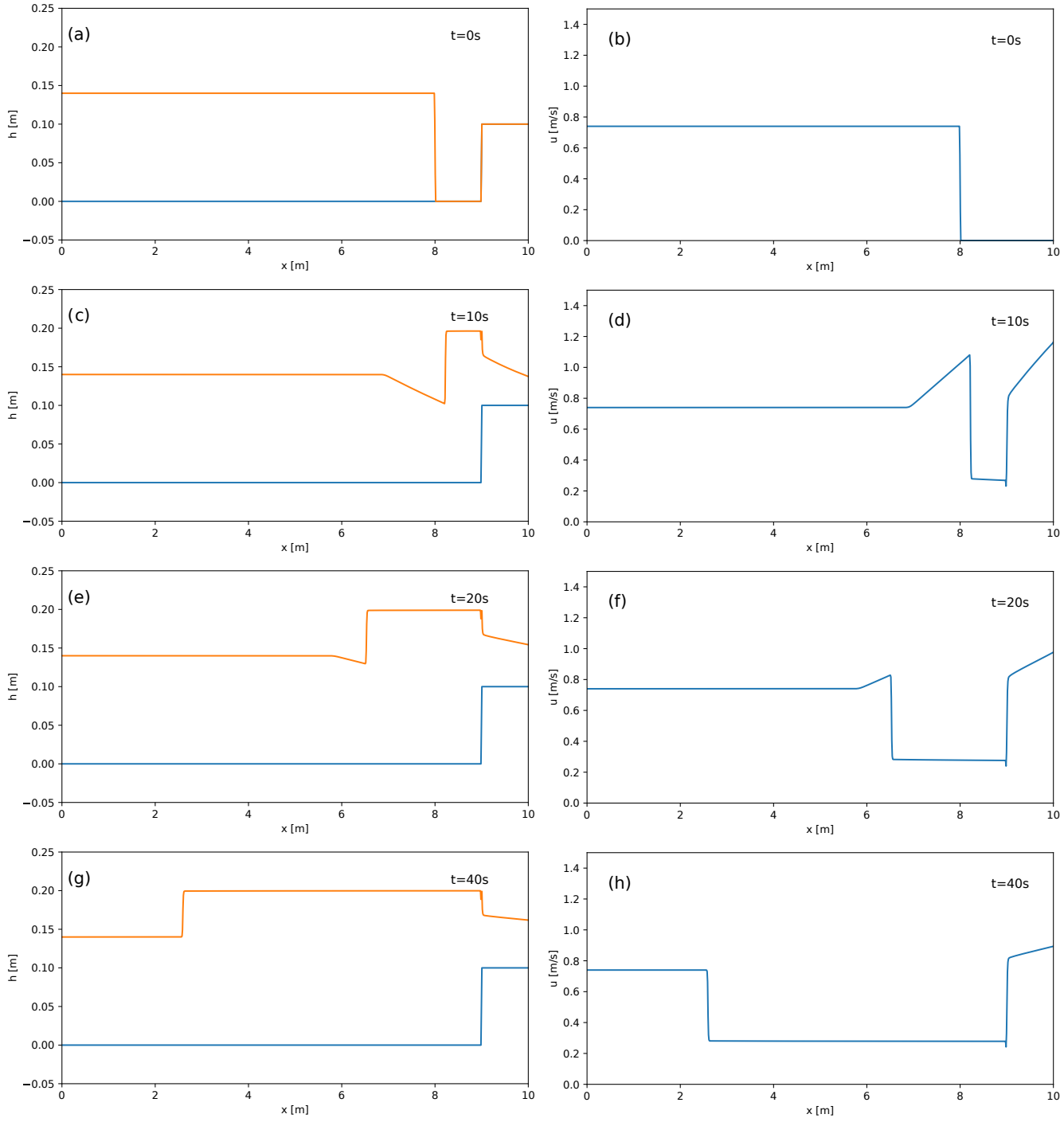

Figure 4. Thickness (left) and velocity (right) profiles for a one-dimensional subcritical flow with a backward propagating hydraulic jump.

5.2 Radial ash flow

In this section we apply the new model to reproduce results presented in Engwell et al. (2016) for large dilute flows producing coignimbrite columns. Thus, in comparison to the test cases of the previous section, we model a mixture of gas and solid particles, here with a diameter 100 microns. Solid ~~deposition~~ sedimentation and atmospheric air entrainment are also modeled, resulting in a mixture for which temperature and density change during the transport. Engwell et al. (2016) used a steady-state 1D model with radial symmetry, and here we want to reproduce the steady condition with transient 2D simulations. To be consistent with the assumptions of Engwell et al. (2016), and to obtain a steady state, we do not consider any modification of the topography associated with the ~~deposition~~ sedimentation of solid particles. In this way, with a steady source, it is possible to reach a steady condition and a steady radial profile.

The use a steady-state numerical code, as done by Engwell et al. (2016), restricts the study to supercritical flows, and in this section we present numerical simulations for supercritical conditions only. As discussed for the previous example, subcritical and supercritical boundary conditions corresponds to two different physical settings, and different boundary/source conditions are prescribed to model the different initial regimes. In the supercritical regime, flow downstream from the source is controlled by conditions upstream, and all the conservative variables must be fixed at the boundary inlet. This is the case for the two axisymmetric simulations presented in Fig. 5 and Fig. 6, where the initial Richardson numbers are 0.1 and 0.9, respectively. For both simulations the inlet conditions are given at $R = 2000$ m, with the initial thickness fixed at $h = 2000$ m, the initial gas mass fraction at 0.2, the initial temperature at $T = 900$ K and the friction coefficient at 0.001. The initial velocities are computed from the other variables and the Richardson number, resulting in an initial radial velocity of 93.32 m s^{-1} for $Ri = 0.9$ and 279.98 m s^{-1} for $Ri = 0.1$. A 20km by 20km computational domain, discretized with 100m size cells, is used for the two simulations. For both simulations, when the mixture becomes buoyant in a computational cell (due to entrainment and heating of atmospheric air and particle sedimentation), the mass is removed from that cell, while the solution is not computed for the cells that are fully inside the area defined by $R < 2000$ m. The two figures show the flow solution at $t = 200$ s, when a steady condition for both radial flows is reached. In the left panels a 3D view of the flow thickness is presented. The color of the free surface represents flow thickness, clearly showing a lower thickness for the simulation with initial $Ri = 0.9$. When using Cartesian grids to model axisymmetrical flows, it is not obvious that the output of the simulation would produce the correct results in terms of radial symmetry of the flow front. In fact, while the inlet velocity is given analytically at the lateral surface of the inlet cylinder, i.e. at a distance of 2000m from the point (0,0), the boundary conditions are prescribed numerically at the faces of the computational cells, which can be at different distances. For this reason, a correction on the velocity accounting for this discrepancy is applied to each inlet face. Model results, as shown in the left panels, highlight that this correction, coupled with the second-order discretization in space implemented in the model, correctly produce axisymmetric flows.

Plots of thickness and velocity along a radial section are shown in the right panels of Fig. 5 and Fig. 6, for the initial Richardson numbers of 0.1 and 0.9, respectively. These results can be compared with those presented in Engwell et al. (2016), Fig.3, where the same initial parameters have been used. For both initial conditions, model solutions show a decrease in flow thickness immediately after the source which is more pronounced for the largest value of Ri. Then, after approximately 3.5 km

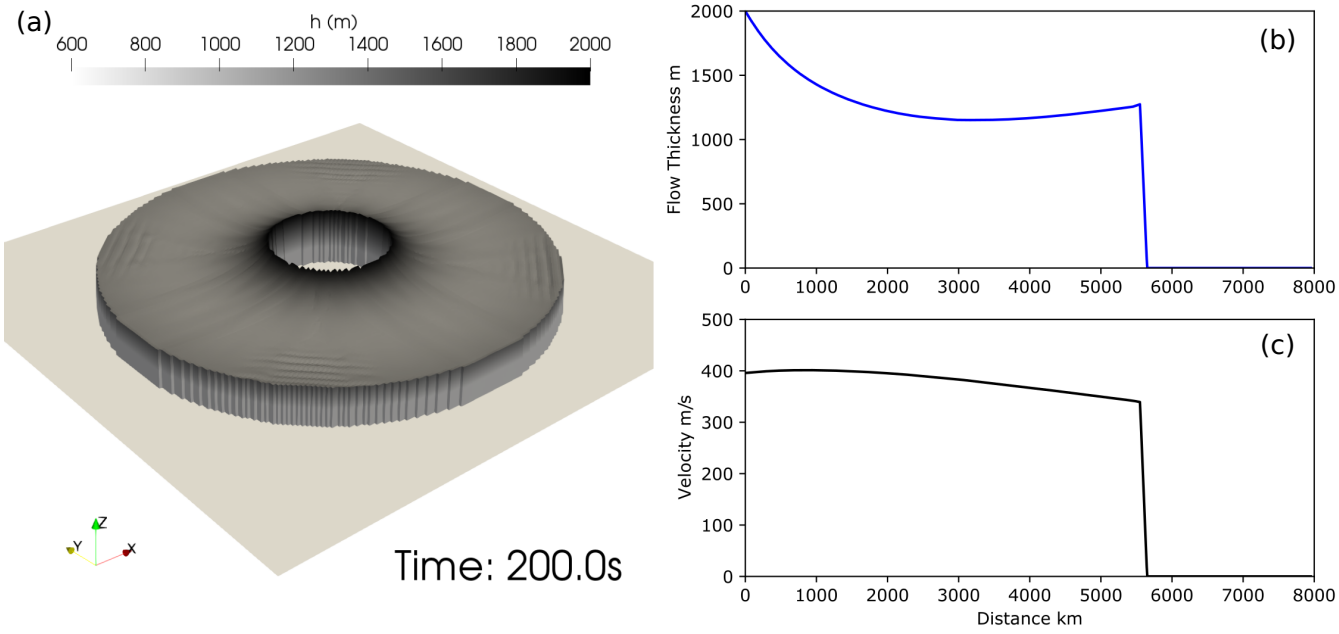

Figure 5. Supercritical flow with initial Ri=0.1. The solution is computed only for the cells of the computational domain outside (fully or partially) $R = 2000$ m. The color of the free surface represents flow thickness.

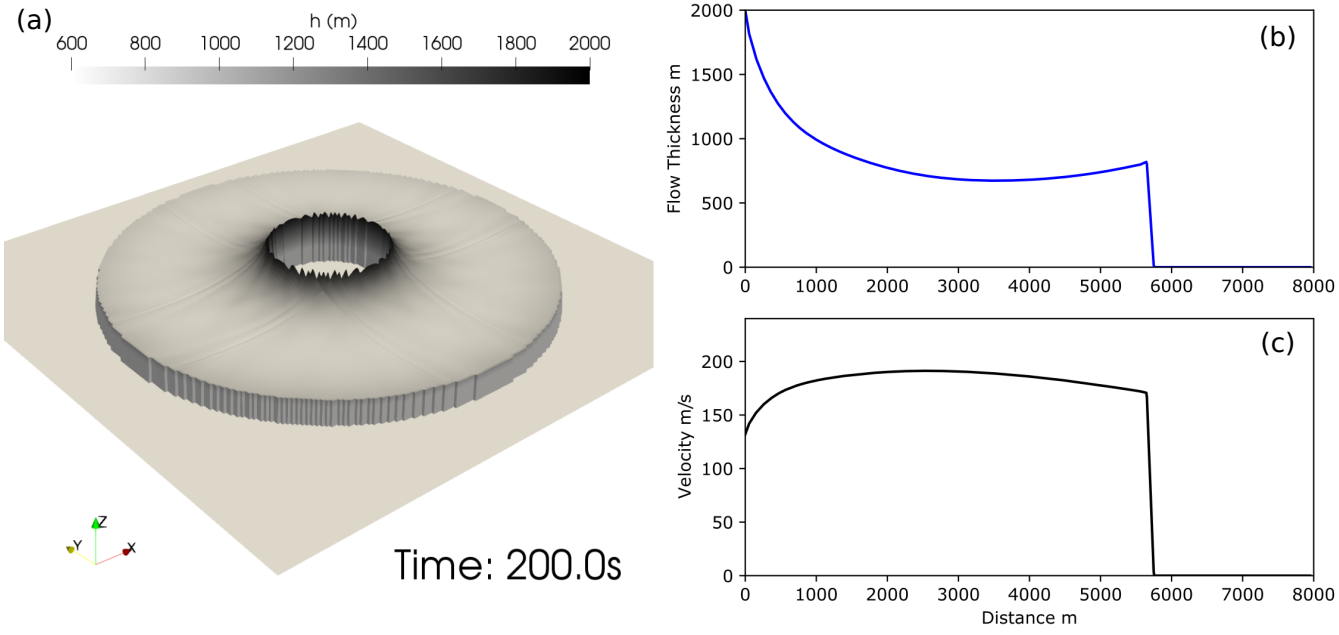

Figure 6. Supercritical flow with initial Ri=0.9. The solution is computed only for the cells of the computational domain outside (fully or partially) $R = 2000$ m. The color of the free surface represents flow thickness.

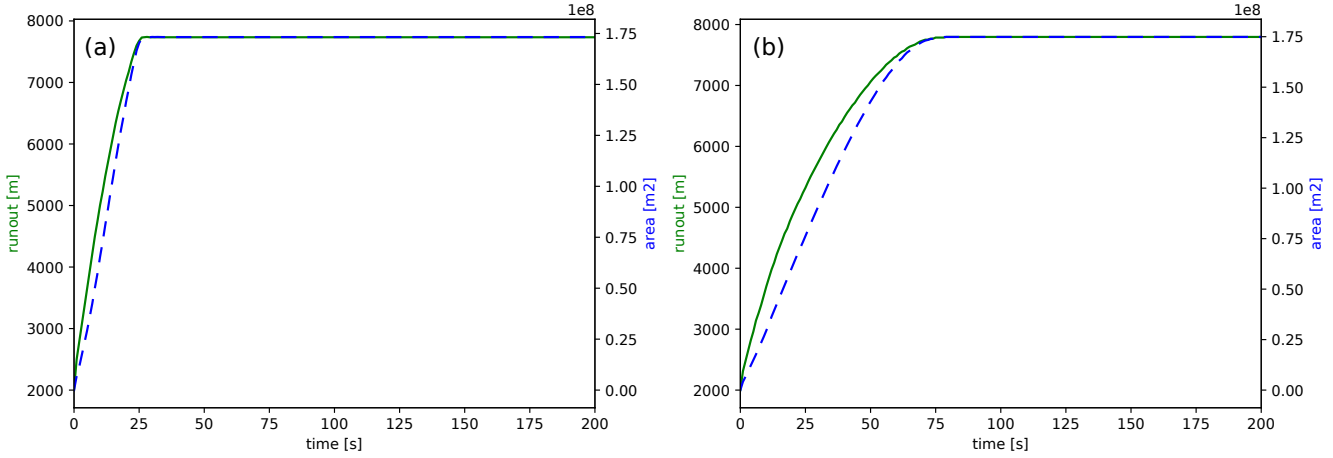

Figure 7. Runout (solid green line) and area invaded (dashed blue line) versus time for a simulation with initial $Ri = 0.1$ (left panel) and $Ri = 0.9$ (right panel).

from the source, thickness increases again. These two different trends are due to the superposition of the thinning associated with the radial spreading and the thickening associated with atmospheric air entrainment, the first being more important close the source and the second at greater distances (see also Calabrò et al., 2022). The velocity profiles of the two simulations present larger differences in the absolute values than the thickness, mostly because of the initial velocities associated with the different Richardson numbers. At the maximum runout distances, which are comparable for the two simulations, this results in a residual momentum for the simulation with $Ri = 0.1$ being almost twice that for the simulation with $Ri = 0.9$, as shown also by (Engwell et al., 2016).

An advantage of a transient model, with respect to a steady one, is that the simulation can provide information on the propagation of the flow and the time needed to reach the maximum runout. Fig. (7) shows the runout (solid green line) and the area invaded by the flow (green blue line) versus time for the two simulations presented above. In both simulations, we observe an almost linear increase in the area invaded with time, up to the time at which the maximum runout is reached. For the simulation with initial $Ri = 0.1$, and thus with a larger flow velocity, the maximum runout is reached at $t = 28$ s, while for the simulation with initial $Ri = 0.9$ it is reached at $t = 79$ s. Furthermore, we remark that only a transient model can simulate the modifications of the topography associated with the ~~deposition~~ sedimentation of solid particles, because of the intrinsic transient nature of this process.

6 PDCs over water: the ~~1883~~ Krakatau ~~eruption~~case study

Here we present an application of the model to the ~~1883 Krakatau eruption, which~~ Krakatau volcano, with inputs informed by the 1883 eruption. This simulation highlights the capability of the model to treat the interaction of the flow with topography, the presence of hydraulic jumps and the vaporization and entrainment of water.

The Krakatau volcanic system is notorious for eruptive behaviour that interacts with the seas of the surrounding Sunda Straits. In 1883, an eruption produced PDCs that propagated more than 40 km across the sea (Carey et al., 1996), impacting populations on the coastlines of Sumatra and Java (Simpkin and Fiske, 1983), and potentially playing a role in the formation of devastating tsunamis that lead to the deaths of > 36000 people (Maeno and Imamura, 2011). Here, we test the flow model on real topography and investigate topographic effects on flow regime and the transition from supercritical to subcritical flow. In addition, we show the effect of ingestion of sea water in the form of water vapour into the flows.

We test the flow over water model formulation using a contemporary (i.e. representing recent topography rather than that in 1883) 30 metres SRTM Void filled DEM (USGS EarthExplorer downloaded July 2021) of the area around the Krakatau volcanic complex and the Sunda Straits (Fig 8). We assume that all cells with an elevation of zero are water. Model inputs were informed using information from the 1883 eruption from the published record and from field analysis of eruption deposits. An initial flow temperature of 773K (500°C) was used based on results from Mandeville et al. (1994). However, the simulations are not aimed at replicating the eruption, but to give insight into the model application and the possible dynamics of these flows. We point out that we do not simulate here the collapse of the explosive column, but only the dilute flow generated by the entrainment of atmospheric air and the collapse of the column. Thus, the initial conditions of the simulation refers to the source conditions of the radially spreading dilute flow. An initial flow radius of 2 km, flow Richardson number of 0.7 and mass flow rate of ~~10^9 m^3~~ 10^{10} kg s^{-1} were used. The initial density is 40 ~~kgm~~kg m^{-3}. Initial flow thickness ~~and velocities~~ ($\approx$ 310 m) and radial velocities ($\approx$ 65 m s^{-1}) were calculated from these parameters. A particle class of 100 microns was used, and the gamma coefficient ($\gamma_{i_s,wv}$) was set to 0.86. This value was not constrained by observations, but selected from an ensemble of simulations to better highlight some features of the flow (large entrainment of water vapour, hydraulic jumps, transient dynamics). Flow parameters were analysed along a number of transects (Fig 8), which have different topographic profiles relating to the islands around the volcano (Fig 9). A probe location is used to show how flow properties at a given location change with time.

The source condition of the simulated PDC mimics the initial radial spreading generated by a column collapse, the flow then quickly interacts with the nearby Krakatau islands of Sertung, Rakata and Panjang. The flow overtops the proximal islands of Sertung and Panjang, but it is directed around the much taller island of Rakata, with the flow fronts merging downstream on the far side of the island (Fig 8). The flow runout at 360 and 1320 seconds varies along the different transects (Figs 10 and 11), with runout considerably less along transects 5 and 6 than the other transects, related to the more variable topographic elevation along these transects (Fig 9). Flow temperature shows a gradual decrease with distance from source along most transects. The temperature drops to 300 k along transect 5 at 360 seconds and transect 6 at 1320 seconds. This reflects that at these times, there is no flow at these locations, and the temperature is that of the ambient.

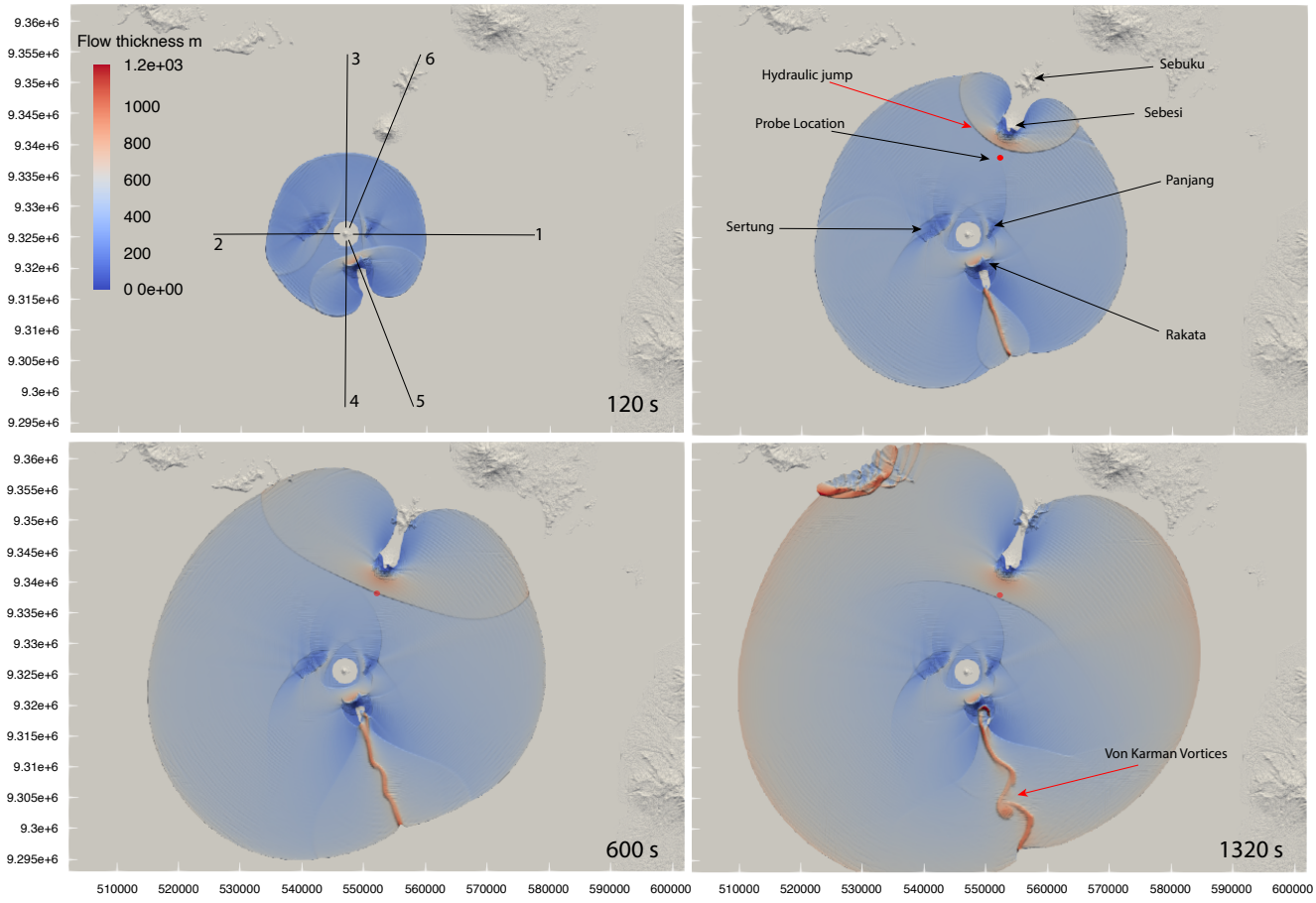

Figure 8. Snapshots of simulation `SA4_0003`, where a grainsize of 100 microns, a MFR of 10^9, and a gamma coefficient ($\gamma_{i_s,wv}$) of 0.86 was used. Each image represents a different time step in the simulation. The red marker shows the probe location at 552669E 9338081N UTM. The topographic elevation for each transect is shown in Figure 9.

In general, the simulated flow develops larger thicknesses at the head (Figs 10, 11), followed by a thinner body. These changes are related to variations in the Ri number, and air entrainment (Figs 10, 11). In comparison to trends seen in Figs 5 and 6, and results shown by ~~Bursik and Woods (1996); Calabrò et al. (2022); Shimizu et al. (2019)~~Bursik and Woods (1996); Calabrò et al. (20 , the trends do not show an initial decrease in thickness with distance. This is the result of the large volume of water vapour entrained into the flow, as shown in Fig 11F. Numerical model results using smaller values for the $\gamma_{i_s,wv}$ coefficient (Supplementary Figure 1) show a decrease in flow thickness with distance from source. Flow thickness considerably increases upstream of topographic barriers, such as the islands of Sertung (transect 2) and Panjang (transect 1), which are within a couple of kilometres of the source. This increase is the result of the formation of backward propagating hydraulic jumps, marking the transition from supercritical flows with Richardson numbers less than one to subcritical flow. Downstream of topographic barriers, when the flows are capable of overcoming the obstacle, they transition back from thick, subcritical to thin supercritical

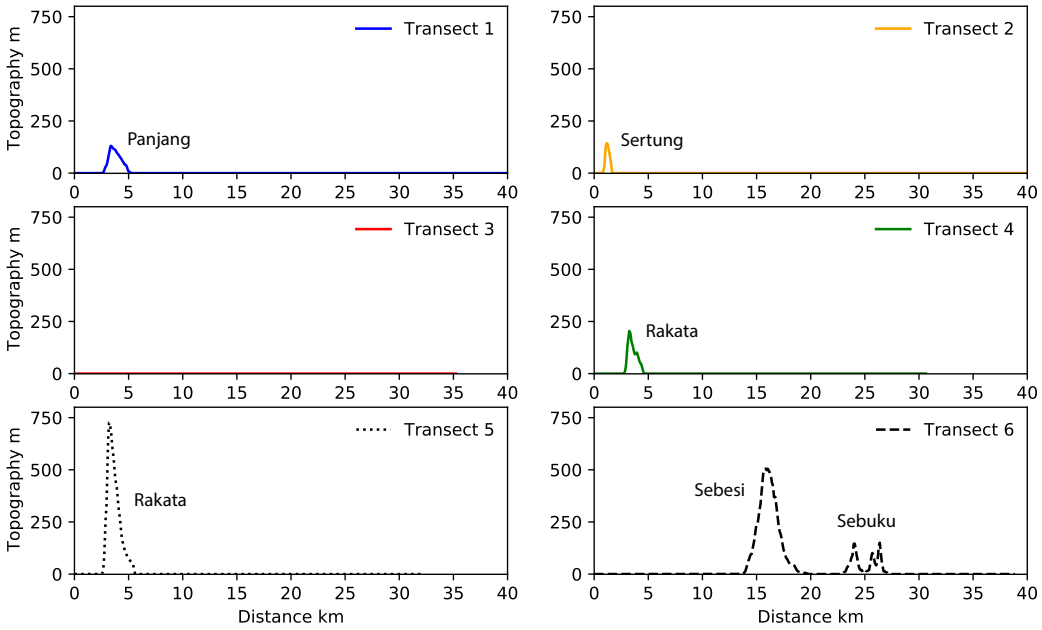

Figure 9. Topographic profiles of transects shown in Figure 8A. Note the vertical exaggeration of the y-axis. Transect 3 is the only transect that does not show variation in elevation along the flow runout, all other transects cross one of the many islands in the Sunda Strait.

flows. The most extreme variation in Richardson numbers occurs along transect 5 at 1320 s, with a high Richardson number upstream of Rakata island, a topographic barrier to the flow, and peaking downstream of the island as the flow converges. This peak in Richardson number is due to a large decrease in velocity, which results in an increased loss of particles and therefore a decrease in solid volume fraction within the flow (Figs 10D).

Downstream of Rakata island (transect 5), the flow thickness at 1320 seconds is highly variable showing multiple peaks and troughs not directly associated with any variation in topography. These thickness variations are the result of the formation of Von Karman vortices that formed in the wake of the topographic high on the island of Rakata, to the SE of the source (Fig 11). Variations in Richardson number for some transects match those shown in 1D simulations presented earlier in the paper (Fig 4), whereby the transition from super to subcritical flow moves upstream through time. This is shown particularly well for transect 6: at 360 seconds, the transition is clearly visible at a distance of approximately 13 km from source (Fig 11), while at 1320 seconds, it is less well defined and occurs approximately 2 km closer to the source (Fig 11). This transition is also evident when studying the flow interactions with Sebesi Island, to the NE (Fig. 8): the shape of the hydraulic jump front changes from tightly curved around the island at 360 seconds, to a more elongate region at 600 seconds to a concave region bending back towards the Krakatau Islands at 1320 seconds. In Fig 8 the backwards propagation of the hydraulic jump is also evident when looking at the relative position of the transition region with respect to the red marker. This marker represents the probe location at which we sampled flow variables with time to show the effect of the passing hydraulic jump on current characteristics. In Fig 12A we

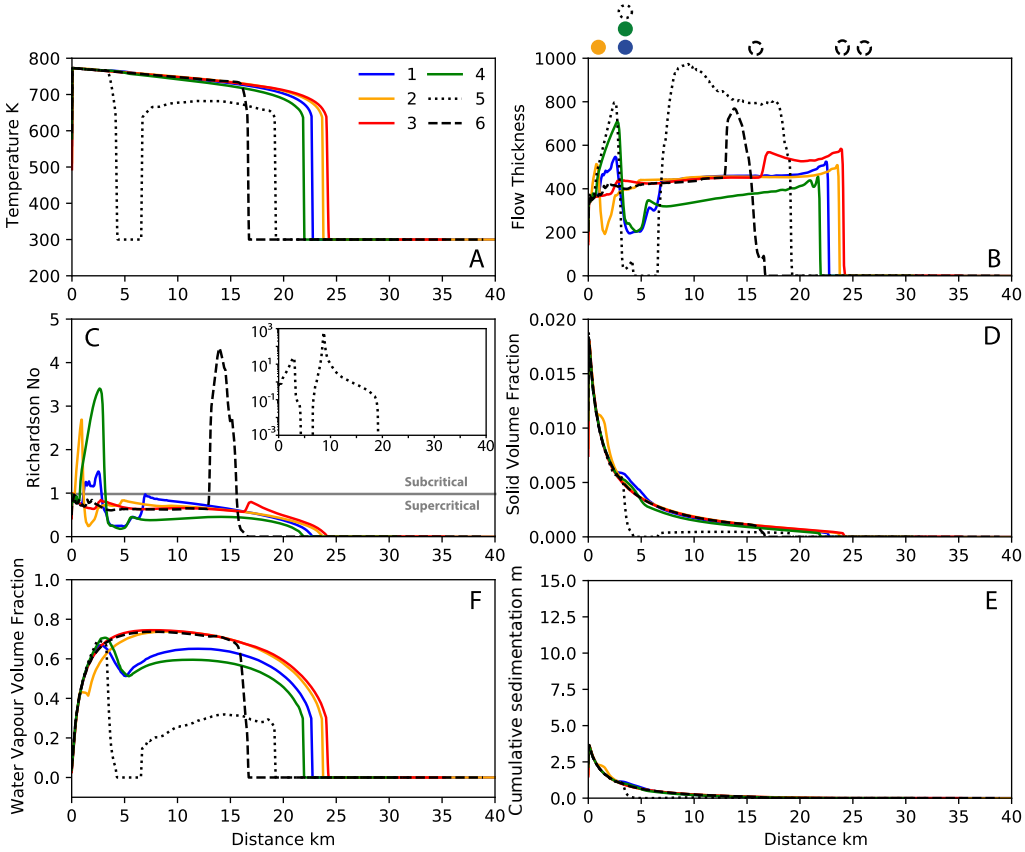

Figure 10. Variation in flow parameters with distance at 360 seconds post flow initiation for simulation `SA4_0003`, along transects shown in Fig 8. Markers above Panel B show the location of topographic barriers for each transect. The Richardson Number with distance for transect 5 is shown in the inset figure.

plot dynamic pressure and in Fig 12B, ~~deposit thickness and deposition~~ cumulative sedimentation and sedimentation rate with time. These figures clearly show the arrival of the flow at 130s. The dynamic pressure also shows the passing of the hydraulic jump at approximately 600 s (as also shown in Fig. 8C). The dynamic pressure shows a sharp decrease at approx. 1900 s, 100 s after source emission ends. Flow arrival at the probe location is also shown in Fig 12B, with an increase in flow thickness and ~~deposition~~ sedimentation rate. After arrival of the flow, the ~~deposition~~ sedimentation rate is almost constant, resulting in a linear increase in deposit thickness with time, with no change associated with transition from supercritical to subcritical flow. The decay in ~~deposition~~ sedimentation rate associated with the cessation of the flow is much more gentle than that of dynamic pressure. Variations in flow characteristics also occur along transect 3. At 360 seconds, transect 3 (Fig 10B) shows a sharp increase in thickness at a distance of 16 km from source that at later stages develops into a backward propagating hydraulic jump. Fig 9 shows flat topography for this transect, but analysis of Fig 8 shows that the increase in thickness is related to the flow interaction with the island of Sebesi.

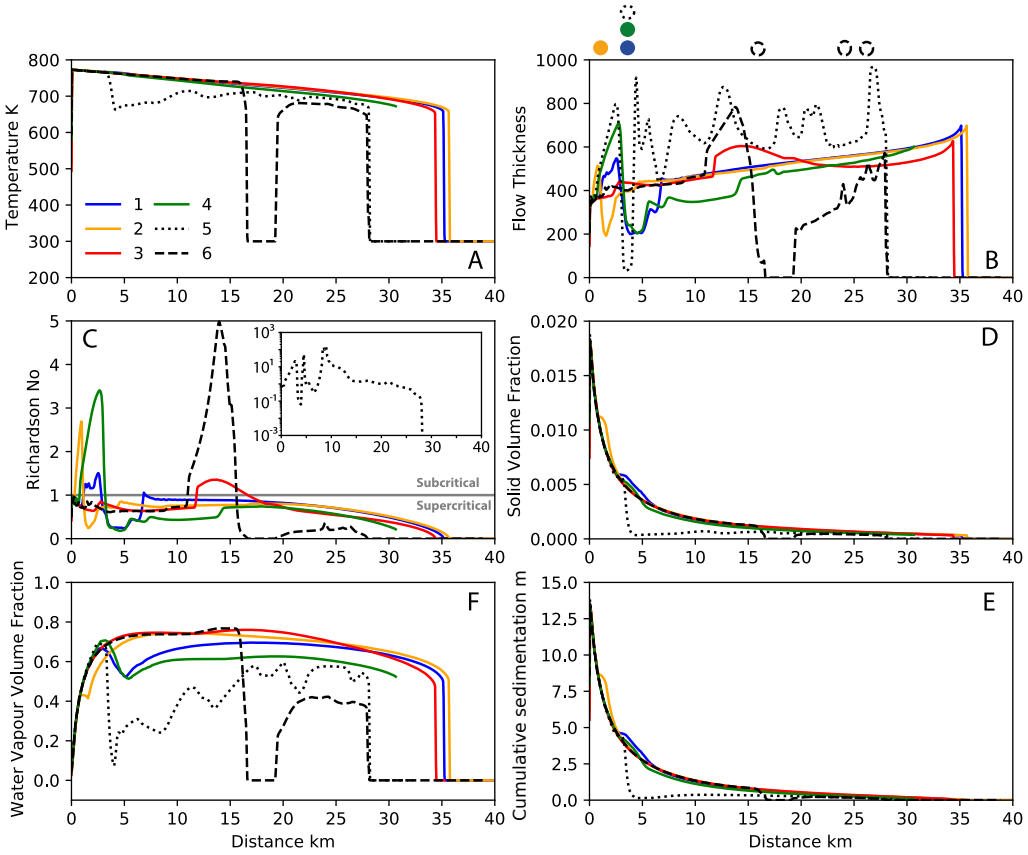

Figure 11. Variation in flow parameters with distance at 1320 seconds post flow initiation for simulation `SA4_0003`, along transects shown in Fig 8. Markers above Panel B show the location of topographic barriers for each transect. The Richardson Number with distance for transect 5 is shown in the inset figure.

Trends in deposit thickness closely follow those in solid volume fraction: both decrease exponentially with distance from source (Figs 10 and 11). Solid volume fraction and deposit thickness have slightly lower decay rates at distances of less than 2 km and 5 km for transect 1 and 2 respectively, and more subtly for transect 4 at distances of approximately 5 km. These increases relate to locations where the flow is in a subcritical regime, i.e. the flow is thicker and has higher Richardson numbers, equivalent to lower velocities. These slightly higher values of solid volume fraction, and consequently ~~deposition~~ sedimentation rates (see Eq. 19) are related to flow interaction with topography, whereby the flow slows and thickens, and has higher ~~deposition~~ sedimentation upstream of barriers. Solid volume fraction and deposit thickness trends differ significantly for transect 5, which has large changes in topographic elevation as it crosses the island of Rakata, close to the source. Both profiles show the same decay as seen in the other transects in the first couple of kilometres from source, before decreasing sharply and, at distances of around 10 km from the source, showing a slight increase. These trends can be explained by the flow interaction with Rakata Island, which has a height of > 700 m (Fig 9). The flow is unable to overtop this barrier, and instead flows around

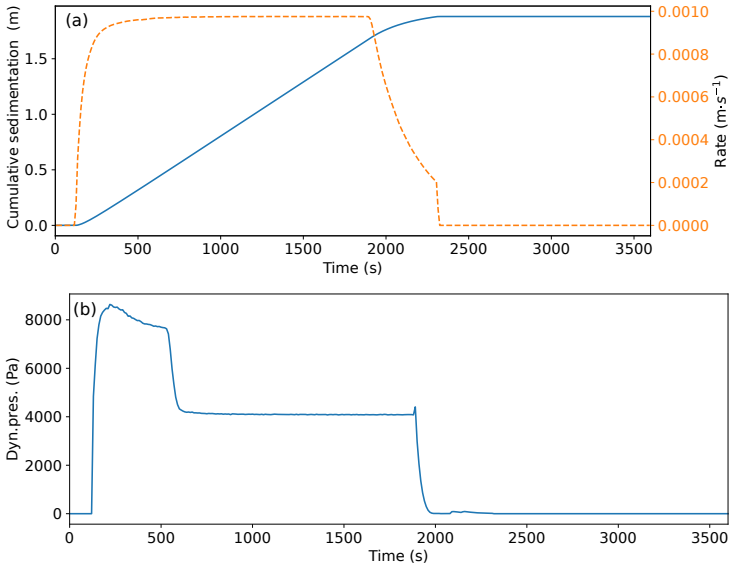

Figure 12. Variation in deposit thickness, rate and dynamic pressure at the probe location shown in Fig 8.

it, converging downstream. The decrease to zero solid volume fraction and deposit thickness represents the sheltered part of Rakata island that the flow does not reach (Figs 10 and 11).

Fig 10F and 11F show a general increase and then decrease in water vapour volume fraction of the flow with distance from source. This is shown in greater detail in Fig 13 where water vapour volume fraction is plot alongside the volume fractions of the other flow components. For the $\gamma_{i_s,wv}$ coefficient used in this simulation, we can see that along both transects, the water vapour volume fraction can reach large values up to almost 0.75. The relative amounts of water vapour and atmospheric air also varies as the flows interact with topography, with transect 1 showing a decrease in water vapour and an increase in entrained air as the flow travels over Panjang island to the east. Transect 3 shows steady variations in water vapour and entrained air, with water vapour volume fraction quickly increasing and entrained air decreasing in the first couple of kilometres. There is then a gradual decrease in the amount of water vapour, and an increase in entrained air over the next 15 km. This is related to a decrease in temperature towards the flow front, which results in lower thermal energy of the depositing particles available for sea water vaporisation. The sharp decrease in water vapour and increase in air corresponds to the flow front. Transect 3 does not intersect any topography, resulting in consistent trends with distance from source at 360 seconds. However, at 1320 seconds, some subtle variation in both water vapour (a slight decrease) and entrained air volume (a slight increase) fraction are seen between 10 and 15 km from source. This is the result of the changing shape of the hydraulic jump that formed around the island of Sebesi. Additional simulations were performed to show the effect of $\gamma_{i_s,wv}$ coefficient of flow characteristics and relevant figures are available in the supplementary materials.

A thorough discussion about the optimal choice of the rheological model and input parameters for PDCs, in particular those over water, requires an extensive comparison with phenomena and events at numerous volcanoes to accurately inform input

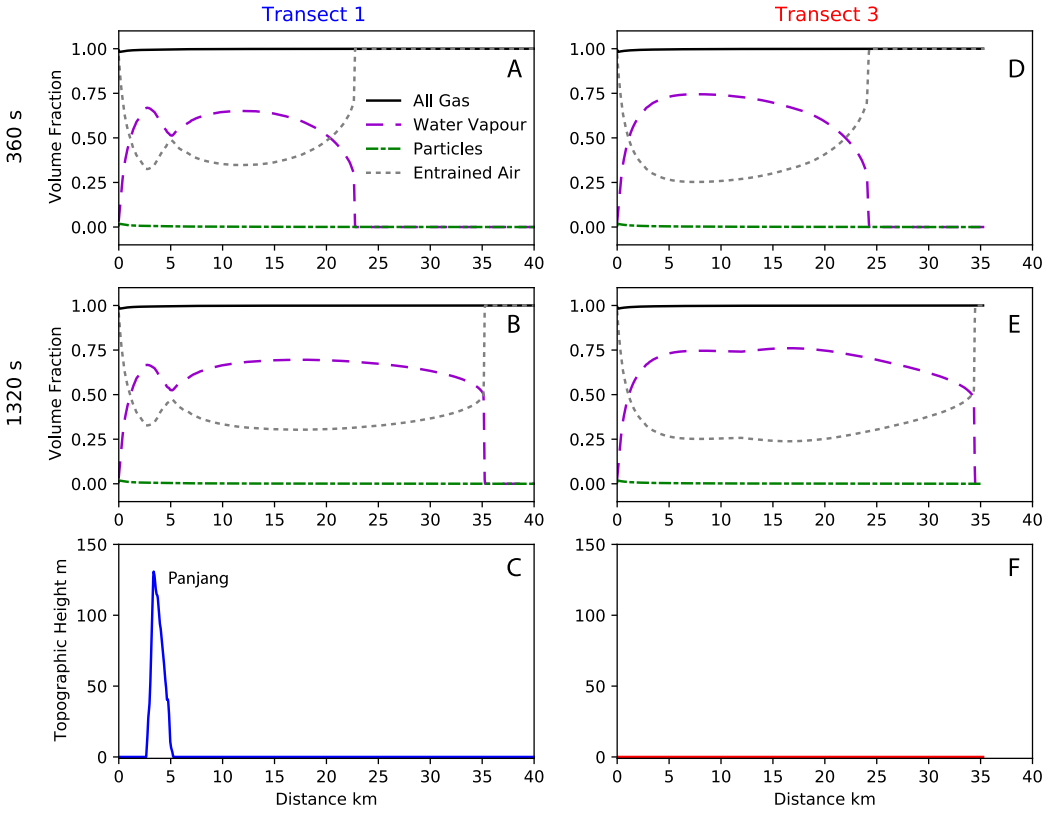

Figure 13. Variation in volume fraction of flow components along transects 1 and 3 at 360 and 1320 seconds post flow initiation.

parameters, and where sufficient observations are available with which to validate model results. More accurate measurements are needed to achieve a better calibration of the model. This, however, is beyond the scope of the present work.

7 Conclusions

We have presented ~~the developments of~~ developments to the physical model and the open source numerical code IMEX_SfloW2D (de' Michieli Vitturi et al., 2019). They consist of the generalization of the shallow-water equations to describe a polydisperse fluid-solid mixture, including terms for sedimentation and entrainment of solids and water vapour, transport equations for solid particles of different sizes, transport equations for different components of the carrier phase, and an equation for temperature/energy. Constitutive equations allow us to adapt the numerical code to solve different types of geophysical mass flows (landslides, debris flows, lahars, snow and rock avalanches, pyroclastic avalanches) and here we have presented its application to the simulation of transient PDCs. The model resolves the depth-averaged flow velocity and density, and does not account for the effects of internal flow stratification. In particular, it cannot be applied to PDCs in which the basal, concentrated flow interacts with the overlaying dilute ash cloud in a two-layer system (Shimizu et al., 2019). It is therefore suited to describe

PDCs end-members (either a concentrated pyroclastic avalanche or an inertial PDC). The numerical code has been tested to verify its capability to describe both sub- and supercritical regimes, as appropriate for large-scale, ignimbrite forming eruptions. The results of synthetic numerical benchmarks demonstrate the robustness of the numerical code facing trans-critical flows. Moreover, they highlight the importance of simulating transient in comparison to steady-state flows, and flows in 2D versus 1D currents. Finally, the example application to ~~the Krakatau 1883 eruption~~Krakatau volcano, shows the capability of the numerical model to face a complex natural case involving the propagation of PDCs over the sea surface and across topographic obstacles, showing the relevance, at the large scale, of non-linear fluid dynamic features, such as hydraulic jumps and Van Karman vortices. It is important to remark that, even if the 2D applications presented here are for radially spreading flows, the code is not restricted to these kind of flows, but can applied, with the proper inlet conditions, to any kind of flow over a 2D topography.

In future versions of the code we plan to adapt an approach similar to that presented for Newtonian laminar flows in (Biagioli et al., 2021), where the depth-average equations have been modified to account for the vertical variation of velocity and temperature. The proposed modifications were implemented in the first version of IMEX-SfloW2D, and the applicability of such approaches to velocity and particle concentration profiles for dilute pyroclastic density currents has been shown in (Keim and de' Michieli Vitturi, 2022). Furthermore, in order to extend the range of the applications of the model and to allow for the numerical discretization of non-conservative terms, as those appearing in multi-layer models and in approaches proposed in (Fyhn et al., 2019) for the simulation of the constant velocity phase of channelized flows, we plan to implement the finite-volume schemes proposed in (Diaz et al., 2019) in the code. We also point out that the present version of the code implements a rather simplified model for particle settling velocity, and in the future we plan to adopt more recent and accurate treatments for its calculations. For simple spheres, as assumed here, there are drag laws that avoid the jump in the Lun and Gidaspow drag law (Clift and Gauvin, 1971; Haider and Levenspiel, 1989), which can result in numerical problems when velocity is computed with an iterative numerical scheme. In addition, the use of a drag law for spheres in the case of natural sediments/volcanic particles is an important simplification that can lead to overestimating the terminal velocity, hence the sedimentation rate in the flow. We remark that the adoption of more complex models (Ganser, 1993; Bagheri and Bonadonna, 2016; Diogua would also require the knowledge of additional parameters characterizing the shape of the particles, which are not always easy to retrieve.

In conclusion, the depth-averaged model introduced in this study offers a promising avenue for advancing probabilistic volcanic hazard assessment. By providing a computationally efficient alternative to traditional 3D models, it significantly reduces the computational burden while still capturing, as shown by the Krakatau application, essential aspects of volcanic flows. For instance, for the simulation of the Krakatau case study for 1800 seconds, the code required 2 hours of computational time on a 7th Generation Kaby Lake Intel Core i7 processor, which could be substantially reduced with a parallel run on multiple cores. Moreover, the utilization of a High-Performance Computing (HPC) system further amplifies the potential of the depth-averaged model in probabilistic volcanic hazard assessment, enabling the execution of a large number of simulations within a reasonable timeframe. This makes the model well-suited for practical applications where timely hazard assessment is crucial.

Code availability. The numerical code, benchmark tests and documentation are available at https://github.com/demichie/IMEX_SfloW2D_v2 (last access: 16 December 2022). Preprocessing scripts (to change the grid resolution and the numerical schemes) and post-processing scripts (to plot the solution variables and to create animations) are also available. Furthermore, some of the examples presented in this paper have a page description on the model Wiki (https://github.com/demichie/IMEX_SfloW2D_v2/wiki, last access: 16 December 2022), where detailed information on how to run the simulations is given. The digital object identifier (DOI) for the version of the code documented in this paper is https://doi.org/10.5281/zenodo.7476737.

Appendix A: Derivation of depth-averaged governing equations for variable density flows

In this appendix we present the derivation of the depth-averaged momentum and energy equations. For the sake of simplicity, we present the derivation by considering the ordinary gravity g, instead of the reduced gravity g', and without friction terms. Furthermore, we present the derivation for a flow over a 1D topography parallel to the x axis. In this case, $B = B(x,t)$ and $h = h(x,t)$ are function of x and t only, and the velocity vector is $\mathbf{v} = (u, w)$, where u and w are the horizontal and vertical components, respectively (see Fig. A1).

A1 Momentum equation

The momentum equation is derived by integrating the Navier-Stokes equations in conservative form over the thickness of the flow, and by applying appropriate boundary conditions at the top (free surface) and the bottom (topography) of the flow.

For a flow with no mass exchange with the surrounding environment and over an impermeable terrain constant in time ($\frac{\partial B}{\partial t} = 0$), the following kinematic conditions at the free surface and at the flow bottom (Johnson, 1997) are usually employed:

$$\frac{\partial (B+h)}{\partial t} = w(x, B+h, t) - u(x, B+h, t)\frac{\partial (B+h)}{\partial x}$$

$$w(x, B, t) - u(x, B, t)\frac{\partial B}{\partial x} = 0.$$

The first condition states that the (moving) free-surface must be always composed of fluid particles, i.e. that the free-surface elevation changes at a rate equal to the velocity of the flow in the direction perpendicular to the surface. The second condition states that the fluid velocity directed perpendicular to a solid boundary must vanish on the boundary itself.

However, here we consider atmospheric air entrainment and solid sedimentation, which affect both the topography and the free-surface elevations. For this reason, the classical equations presented above are modified in the following way:

$$\frac{\partial B}{\partial t} + u(x, B, t)\frac{\partial B}{\partial x} - w(x, B, t) = \sum_{i_s=1}^{n_s} \underline{D}\underline{S}_{s,i_s},$$

$$\frac{\partial (B+h)}{\partial t} + u(x, B+h, t)\frac{\partial (B+h)}{\partial x} - w(x, B+h, t) = E_a.$$

In a 2D static Eulerian frame of reference (see Fig. A1), the momentum equation for horizontal component of the velocity for a generic fluid parcel at the point (x, z) and with velocity (u, w), without shear stress and external forces, writes in the

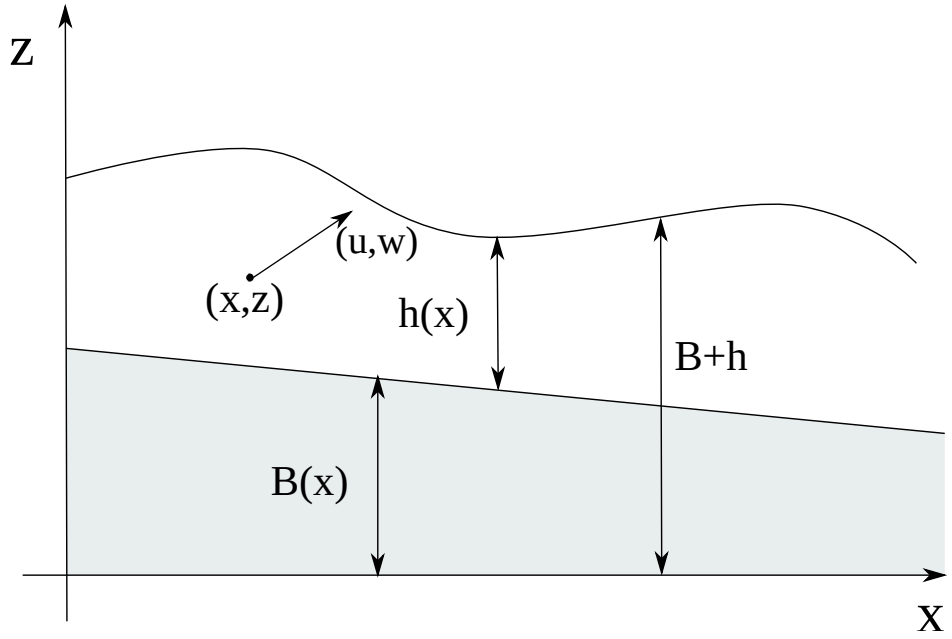

Figure A1. Model variables for a 1D flow. B is the topography elevation, h denotes flow thickness and u and w are the horizontal and vertical components at the point (x, z).

following way (Anderson and Wendt, 1995, Eq. 2.42a):

$$\frac{\partial(\rho_m u)}{\partial t} + \frac{\partial(\rho_m u^2)}{\partial x} + \frac{\partial(\rho_m uw)}{\partial y} = -\frac{\partial p}{\partial x}. \tag{A.1}$$

If we integrate between B and $B+h$ on both sides of the equation, we can apply the Leibniz rule to the first term of the vertically integrated momentum conservation equation, obtaining:

$$\int_B^{B+h} \frac{\partial(\rho_m u)}{\partial t} dt = \frac{\partial}{\partial t} \int_B^{B+h} \rho_m u dz + \rho_m u(B)\frac{\partial B}{\partial t} - \rho_m u(B+h)\frac{\partial(B+h)}{\partial t} =$$
$$\frac{\partial}{\partial t}(\rho_m h\bar{u}) + \rho_m u(B)\frac{\partial B}{\partial t} - \rho_m u(B+h)\frac{\partial(B+h)}{\partial t},$$

where in the last equality we assumed that the density does not vary with depth, and where we denoted with $\bar{u}$ the depth-averaged horizontal velocity:

$$\bar{u} = \frac{1}{h}\int_B^{B+h} u dz.$$

In a similar way, we apply the Leibniz rule to the integral of the second term on the left-hand side of the momentum equation:

$$\int_B^{B+h} \frac{\partial(\rho_m u^2)}{\partial x} dz = \frac{\partial}{\partial x} \int_B^{B+h} \rho_m u^2 dz + \rho_m u^2(B) \frac{\partial B}{\partial x} - \rho_m u^2(B+h) \frac{\partial (B+h)}{\partial x} =$$

$$\frac{\partial(\rho_m h \bar{u^2})}{\partial x} + \rho_m u^2(B) \frac{\partial B}{\partial x} - \rho_m u^2(B+h) \frac{\partial (B+h)}{\partial x}$$

where we denoted with $\bar{u^2}$ the depth-averaged value of the square of the horizontal velocity:

$$\bar{u^2} = \frac{1}{h} \int_B^{B+h} u^2 dz.$$

For the integral of the last term on the left-hand side of the momentum equation we can apply the fundamental theorem of calculus:

$$\int_B^{B+h} \frac{\partial \rho_m uw}{\partial z} dz = \rho_m u(B+h) w(B+h) - \rho_m u(B) w(B).$$

Thus, by summing the three terms, the integral of the left-hand side of the momentum equation ~~A.1~~ (A.1) is:

$$\frac{\partial}{\partial t}(\rho_m h \bar{u}) + \frac{\partial}{\partial x}(\rho_m h \bar{u^2}) + \rho_m \tilde{u}(B) \left[\frac{\partial B}{\partial t} + u(B) \frac{\partial B}{\partial x} - w(B) \right]$$
$$- \rho_m \tilde{u}(B+h) \left[\frac{\partial (B+h)}{\partial t} + w(B+h) - u(B+h) \frac{\partial (B+h)}{\partial x} \right].$$

In the previous equation, we denoted with the symbol $\tilde{u}$ the horizontal velocities at the bottom and at the free surface interfaces. It is important to observe that at each of these interfaces we have two different velocities, one internal to the fluid and one external, and $\tilde{u}$ represents the velocity that contribute to the change in the terrain elevation or in the free-surface elevation. The first one changes because of particle sedimentation from the flow, so the velocity to consider is that of the flow. Conversely, the free-surface elevation change is associated with entrainment of atmospheric air, which we assume still. For this reason, $\tilde{u}(B+h) = 0$, and the last term is neglected, resulting in a simpler form of the integral of the left-hand side of the momentum equation:

$$\frac{\partial}{\partial t}(\rho_m h \bar{u}) + \frac{\partial}{\partial x}(\rho_m h \bar{u^2}) + \rho_m u(B) \sum_{i_s=1}^{n_s} \underset{\sim}{DS}_{s,i_s}$$

For the integral of the right-hand side of the momentum equation (pressure term), we assume an hydrostatic pressure profile, i.e.:

$$p(x,z,t) = \int_z^{B+h} \frac{\partial p(x,z,t)}{\partial z} dz = \rho g (B+h-z) \tag{A.2}$$

To integrate the pressure term, we apply again the Leibniz rule to compute the term

$$\int_B^{B+h} \frac{\partial p(x,z,t)}{\partial x} dz = \frac{\partial}{\partial x} \int_B^{B+h} p(x,z,t) dz + p(x,B,t) \frac{\partial B}{\partial x}$$

$$-p(x,B+h,t) \frac{\partial}{\partial x}(B+h) = \frac{\partial}{\partial x} \left[-\rho_m g \frac{(B+h-z)^2}{2} \right]_B^{B+h} + \rho_m g h \frac{\partial B}{\partial x}$$

$$= -\frac{\partial}{\partial x} \left[\rho_m g \frac{h^2}{2} \right] + \rho_m g h \frac{\partial B}{\partial x}$$

If we assume that the vertical variations of the horizontal velocity are negligible, we can replace $\bar{u}$ and $\bar{u^2}$ with u and u^2, respectively, where u represents the depth-averaged horizontal component of the velocity. With this assumption, combining the expression obtained for the integral of the left- and right-hand side of the momentum equation, we obtain the following equation:

$$\frac{\partial}{\partial t}(\rho_m h u) + \frac{\partial}{\partial x}(\rho_m h u^2) = -\rho_m u \sum_{i_s=1}^{n_s} DS_{s,i_s} + \frac{\partial}{\partial x} \left[\rho_m g \frac{h^2}{2} \right] - \rho_m g h \frac{\partial B}{\partial x}. \tag{A.3}$$

In Eq. (A.2), for the sake of simplicity, we neglected the contribution of the atmospheric pressure in the hydrostatic pressure, by assuming that the pressure is null at the free-surface. When the contribution of the atmospheric pressure is considered, we obtain an equation with the reduced gravity instead of the ordinary gravity.

A2 Derivation of energy equation for variable density flows

In this appendix we present the derivation of the the depth-averaged total energy equation, under the same assumption that led to the derivation of the depth-averaged momentum equation.

The desired equation is obtained by integrating over the flow depth the total energy equation for a 2D flow without shear stress (Anderson and Wendt, 1995, Eq. 2.64):

$$\frac{\partial}{\partial t} \left[\rho_m \left(e + \frac{u^2+w^2}{2} \right) \right] + \frac{\partial}{\partial x} \left[\rho_m \left(e + \frac{u^2+w^2}{2} \right) u \right]$$
$$+ \frac{\partial}{\partial z} \left[\rho_m \left(e + \frac{u^2+w^2}{2} \right) w \right] = -\frac{\partial (up)}{\partial x} - \frac{\partial (wp)}{\partial z} + w \rho_m g.$$

where $e = C_v T$ is the internal energy of the flow.

By using the Leibniz rule, the integral of the first term of the left-hand side of the energy equation is:

$$\int_B^{B+h} \frac{\partial}{\partial t} \left[\rho_m \left(e + \frac{u^2+w^2}{2} \right) \right] dz = \frac{\partial}{\partial t} \int_B^{B+h} \left[\rho_m \left(e + \frac{u^2+w^2}{2} \right) \right] dz$$
$$+ \left[\rho_m \left(e + \frac{u^2+w^2}{2} \right) \right]_{z=B} \frac{\partial B}{\partial t} - \left[\rho_m \left(e + \frac{u^2+w^2}{2} \right) \right]_{z=B+h} \frac{\partial (B+h)}{\partial t}$$

Proceeding in a similar way, the second term can be written as:

$$\int_B^{B+h} \frac{\partial}{\partial x}\left[\rho_m\left(e+\frac{u^2+w^2}{2}\right)u\right]dz = \frac{\partial}{\partial x}\int_B^{B+h}\left[\rho_m\left(e+\frac{u^2+w^2}{2}\right)u\right]dz$$
$$\left[\rho_m\left(e+\frac{u^2+w^2}{2}\right)u\right]_{z=B}\frac{\partial B}{\partial x} - \left[\rho_m\left(e+\frac{u^2+w^2}{2}\right)u\right]_{z=B+h}\frac{\partial (B+h)}{\partial x}$$

For the integration of the third term of the left-hand side, we apply the fundamental theorem of calculus:

$$\int_B^{B+h} \frac{\partial}{\partial z}\left[\rho_m\left(e+\frac{u^2+w^2}{2}\right)w\right]dz =$$
$$\left[\rho_m\left(e+\frac{u^2+w^2}{2}\right)w\right]_{z=B+h} - \left[\rho_m\left(e+\frac{u^2+w^2}{2}\right)w\right]_{z=B}$$

If we assume that T and ρ_m and u do not vary with depth, then we can write the left-hand side of the energy equation in the following way

$$\frac{\partial}{\partial t}\left[\rho_m h\left(e+\frac{\overline{u^2}+\overline{w^2}}{2}\right)\right] + \frac{\partial}{\partial x}\left[\rho_m h\left(e\bar{u}+\frac{\overline{u^3}+\overline{uw^2}}{2}\right)\right]$$
$$-\left[\rho_m\left(e+\frac{u^2+w^2}{2}\right)\right]_{z=B+h}\left[\frac{\partial (B+h)}{\partial t}+u(B+h)\frac{\partial (B+h)}{\partial x}-w(B+h)\right]$$
$$+\left[\rho_m\left(e+\frac{u^2+w^2}{2}\right)\right]_{z=B}\left[\frac{\partial B}{\partial t}+u(B)\frac{\partial B}{\partial x}-w(B)\right]$$

As for the momentum equation, we observe that the terms in the square brackets depending on the free-surface and topography elevation are associated with air entrainment and particle sedimentation rates. Furthermore, it is important to remark that air entrainment does not carry any kinetic energy in the flow, but only thermal energy, while both energies are lost due to particle sedimentation. With this in mind, we can rewrite the equation above in the following way:

$$\frac{\partial}{\partial t}\left[\rho_m h\left(e+\frac{\overline{u^2}+\overline{w^2}}{2}\right)\right] + \frac{\partial}{\partial x}\left[\rho_m h\left(e\bar{u}+\frac{\overline{u^3}+\overline{uw^2}}{2}\right)\right]$$
$$-\rho_a C_a T_a E_a + \sum_{i_s=1}^{n_s}\left[\rho_{s,i_s}\left(C_{s,i_s}T+\frac{u(B)^2+w(B)^2}{2}\right)\right]\underline{D}\underset{\sim}{S}_{s,i_s}.$$

We compute now the integral of the pressure and gravitational terms. The first term on the right-hand side of the energy equation can be integrated by applying the Leibniz rule:

$$\int_B^{B+h} \frac{\partial(up)}{\partial x} dz = \frac{\partial}{\partial x} \int_B^{B+h} p(x,z,t)u(x,z,t)dz$$

$$+p(x,B,t)u(x,B,t)\frac{\partial B}{\partial x} - p(x,B+h,t)u(x,B+h,t)\frac{\partial(B+h)}{\partial x} =$$

$$\frac{\partial}{\partial x} \int_B^{B+h} p(x,z,t)u(x,z,t)dz + \rho_m g h u(B)\frac{\partial B}{\partial x}$$

. In the second equality, the last term on the left-hand side is null because we assumed the hydrostatic pressure is null at the free surface. In the equation above, the integral of the product of the pressure and the horizontal velocity is computed by approximating the horizontal velocity with $\bar{u}$ and by substituting $p(z) = \rho_m g(B+h-z)$, obtaining

$$\frac{\partial}{\partial x} \int_B^{B+h} p(x,z,t)\bar{u}(x,t)dz =$$

$$\frac{\partial}{\partial x}\left[u(x,t)\int_B^{B+h} \rho_m g(B+h-z)dz\right] = \frac{\partial}{\partial x}\left[\rho_m g \bar{u}\frac{h^2}{2}\right]$$

The second pressure term on the right-hand side of the energy equation, when integrated over the flow depth, is:

$$\int_B^{B+h} \frac{\partial(wp)}{\partial z} dz = p(x,B+h,t)w(x,B+h,t) - p(x,B,t)w(x,B,t) = -\rho_m g h w(B+h)$$

This term, if we assume that the variations of the vertical component of the velocity with flow depth are negligible, cancels out with the integral of the work done by the gravitational force:

$$\int_B^{B+h} w\rho_m g = \rho_m g h \bar{w}.$$

Now, if we sum all the terms, we have:

$$\frac{\partial}{\partial t}\left[\rho_m h\left(e + \frac{\overline{u^2}+\overline{w^2}}{2}\right)\right] + \frac{\partial}{\partial x}\left[\rho_m h\left(e\bar{u} + \frac{\overline{u^3}+\overline{uw^2}}{2}\right)\right]$$

$$+\frac{\partial}{\partial x}\left[\rho_m g \bar{u}\frac{h^2}{2}\right] = -\rho_m g h u(B)\frac{\partial B}{\partial x}$$

$$-\rho_a C_a T_a E_a + \sum_{i_s=1}^{n_s}\left[\rho_{s,i_s}\left(C_{s,i_s}T + \frac{u(B)^2+w(B)^2}{2}\right)\right] \underline{D}\underset{\sim}{S}_{s,i_s}.$$

If we neglect the contribution of the vertical component of the velocity to the kinetic energy, and we assume that the horizontal velocity is constant ($u(z) = \bar{u}$), we have:

$$\frac{\partial}{\partial t}\left[\rho_m h\left(e+\frac{u^2}{2}\right)\right]+\frac{\partial}{\partial x}\left[\rho_m hu\left(e+\frac{u^2}{2}\right)+\rho_m g u\frac{h^2}{2}\right]=$$
$$-\rho_m ghu\frac{\partial B}{\partial x}+\rho_a C_a T_a E_a-\sum_{i_s=1}^{n_s}\left[\rho_{s,i_s}\left(C_{s,i_s}T+\frac{u(B)^2+w(B)^2}{2}\right)\right]\underline{D}\underset{\sim}{S}_{s,i_s}.$$

By neglecting the vertical component of the velocity we have a small error in the kinetic energy. For this reason, when the equation for the total energy is solved, and the temperature is computed from the total energy, a small error is also present in the temperature.

A3 Derivation of primitive variables from conservative variables

The model solves for the following set of conservative variables:

$$\mathbf{Q}=(Q_1,\ldots,Q_{5+n_s})=(\rho_m h,\rho_m hu,\rho_m hv,\rho_m eh,h\rho_{s_1}\alpha_{s_1},\ldots,h\rho_{s_n}\alpha_{s_n},h\rho_{wv}\alpha_{wv}). \tag{A.4}$$

In order to evaluate the fluxes and the other terms in the governing equations, we need to write, in terms of $(Q_1,\ldots,Q_{4+n_s})$, the primitive variable $\mathbf{P}=(h,hu,hv,T,\alpha_{s_1},\ldots,\alpha_{n_s},u,v)$, which completely define the state. In this appendix we describe the procedure implemented in the code to compute these quantities from the conservative variables.

First of all, mass fractions of solid phases and water vapour are computed as:

$$x_{s,i_s}=\frac{Q_{4+i_s}}{Q_1}\qquad i_s=1,\ldots,n_s\qquad x_{wv}=\frac{Q_{5+n_s}}{Q_1} \tag{A.5}$$

and these allow also to obtain mass fraction of air:

$$x_a=1-\sum_{i_s=1}^{n_S}x_{s,i_s}-x_{wv} \tag{A.6}$$

In this way, mass averaged quantities of the averaged specific heat C_v can be written in the following way:

$$C_{mix}=\sum_{i_s=1}^{n_s}x_{s,i_s}C_{s,i_s}+x_{wv}C_{wv}+x_aC_a \tag{A.7}$$

Once the average specific heat is known, temperature can be computed from the total specific energy, expressed by Q_4, in the following way:

$$h\rho_m C_v T=\left[Q_4-\frac{Q_2^2+Q_3^2}{2Q_1}\right]\Rightarrow T=\frac{1}{Q_1C_v}\left[Q_4-\frac{Q_2^2+Q_3^2}{2Q_1}\right] \tag{A.8}$$

From the temperature it is possible, through the equation of state, to calculate the density of air ($\rho_a=\frac{P}{R_aT}$) and water vapour ($\rho_{wv}=\frac{P}{R_{wv}T}$), and then the density of the mixture:

$$\frac{1}{\rho_{mix}}=\sum_{i_s=1}^{n_s}\frac{x_{s,i_s}}{\rho_{s,i_s}}+\frac{x_a}{\rho_a}+\frac{x_{wv}}{\rho_{wv}} \tag{A.9}$$

Mixture density is used to compute flow thickness and volume fractions:

$$h = \frac{Q_1}{\rho_{mix}}, \quad \alpha_{s,i_s} = \frac{x_{s,i_s}\rho_{mix}}{\rho_{s,i_s}}, \quad \alpha_{wv} = \frac{x_{wv}\rho_{mix}}{\rho_{wv}}, \quad \alpha_a = \frac{x_a\rho_{mix}}{\rho_a} \tag{A.10}$$

Flow velocities are computed from the conservative variables. Here, as done in ..., a desingularizion is applied, in order to avoid division by very small numbers and thus velocities too large.

$$u = \frac{\sqrt{2}Q_1Q_2}{\sqrt{Q_1^4 + \max(Q_1^4, \epsilon)}}, \qquad v = \frac{\sqrt{2}Q_1Q_3}{\sqrt{Q_1^4 + \max(Q_1^4, \epsilon)}}. \tag{A.11}$$

Finally, volumetric fluxes hu and hv are not computed directly from the conservative variables, but from the primitive variables obtained from Eqs. (A.10) and (A.11):

$$hu = h \cdot u, \qquad hu = h \cdot v. \tag{A.12}$$

Author contributions. MdMV has developed the numerical algorithm, implemented the Fortran code and designed the 1D numerical tests. MdMV, TEO and SE contributed to the model formulation and application in the context of volcanological applications. MdMV and SE wrote the manuscript and produced the figures with contributions from TEO.

Competing interests. The contact author has declared that none of the authors has any competing interests.

Disclaimer. TEXT

Acknowledgements. MdMV and TEO were supported by the INGV project Pianeta Dinamico (CUP D53J19000170001) funded by MIUR ("Fondo finalizzato al rilancio degli investimenti delle amministrazioni centrali dello Stato e allo sviluppo del Paese," legge 145/2018), Tema 8-PANACEA. SLE was supported by a Horizon2020 Eurovolc Transnational Access Grant and funding from NERC Grants NE/T002026/1 and NE/S003509/1. The authors also thank the two reviewers (F. Dioguardi and K. Kelfoun) whose valuable comments and feedback greatly enriched the quality of this work.

References

Ancey, C.: Powder snow avalanches: Approximation as non-Boussinesq clouds with a Richardson number–dependent entrainment function, Journal of Geophysical Research: Earth Surface, 109, 2004.

Anderson, J. D. and Wendt, J.: Computational fluid dynamics, vol. 206, Springer, 1995.

Arakawa, A.: Computational design for long-term numerical integration of the equations of fluid motion: Two-dimensional incompressible flow. Part I, Journal of computational physics, 135, 103–114, 1997.

Arakawa, A. and Lamb, V. R.: Computational design of the basic dynamical processes of the UCLA general circulation model, General circulation models of the atmosphere, 17, 173–265, 1977.

Arakawa, A. and Lamb, V. R.: A potential enstrophy and energy conserving scheme for the shallow water equations, Monthly Weather Review, 109, 18–36, 1981.

Bagheri, G. and Bonadonna, C.: On the drag of freely falling non-spherical particles, Powder Technology, 301, 526–544, 2016.

Bartelt, P., Salm, L. B., and Gruberl, U.: Calculating dense-snow avalanche runout using a Voellmyfluid model with active/passive longitudinal straining, Journal of Glaciology, 45, 242–254, https://doi.org/10.3189/002214399793377301, 1999.

Biagioli, E., Vitturi, M. d. M., and Di Benedetto, F.: Modified shallow water model for viscous fluids and positivity preserving numerical approximation, Applied Mathematical Modelling, 94, 482–505, 2021.

Bonnecaze, R. T., Huppert, H. E., and Lister, J. R.: Particle-driven gravity currents, Journal of Fluid Mechanics, 250, 339–369, 1993.

Bouchut, F. and Westdickenberg, M.: Gravity driven shallow water models for arbitrary topography, Communications in Mathematical Sciences, 2, 359–389, 2004.

Branney, M. J. and Kokelaar, P.: Pyroclastic density currents and the sedimentation of ignimbrites, Geological Society of London, https://doi.org/https://10.1144/GSL.MEM.2003.027, 2002.

Bürger, R. and Wendland, W. L.: Sedimentation and suspension flows: Historical perspective and some recent developments, Journal of Engineering Mathematics, 41, 101–116, 2001.

Bursik, M. I. and Woods, A. W.: The dynamics and thermodynamics of large ash flows, Bulletin of Volcanology, 58, 175–193, https://doi.org/10.1007/s004450050134, 1996.

Calabrò, L., Esposti Ongaro, T., Giordano, G., and de' Michieli Vitturi, M.: Reconstructing Pyroclastic Currents' Source and Flow Parameters from Deposit Characteristics and Numerical Modelling: The Pozzolane Rosse Ignimbrite case study (Colli Albani, Italy), Journal of Geophysical Research: Solid Earth, p. e2021JB023637, 2022.

Capra, L., Norini, G., Groppelli, G., Macías, J. L., and Arce, J. L.: Volcanic hazard zonation of the Nevado de Toluca volcano, México, Journal of Volcanology and Geothermal Research, 176, 469–484, 2008.

Carey, S., Sigurdsson, H., Mandeville, C., and Bronto, S.: Pyroclastic flows and surges over water: an example from the 1883 Krakatau eruption, Bulletin of Volcanology, 57, https://doi.org/10.1007/BF00304435, 1996.

Chow, V.: Open-channel hydraulics, 1959.

Christen, M., Kowalski, J., and Bartelt, P.: RAMMS: Numerical simulation of dense snow avalanches in three-dimensional terrain, Cold Regions Science and Technology, 63, 1–14, 2010.

Clift, R. and Gauvin, W.: Motion of entrained particles in gas streams, The Canadian Journal of Chemical Engineering, 49, 439–448, 1971.

Costa, A. and Macedonio, G.: Numerical simulation of lava flows based on depth-averaged equations, Geophysical Research Letters, 32, 2005.

Cushman-Roisin, B. and Beckers, J.-M.: Introduction to geophysical fluid dynamics: physical and numerical aspects, Academic press, 2011.

de' Michieli Vitturi, M. and Pardini, F.: PLUME-MoM-TSM 1.0. 0: a volcanic column and umbrella cloud spreading model, Geoscientific Model Development, 14, 1345–1377, 2021.

de' Michieli Vitturi, M., Esposti Ongaro, T., Lari, G., and Aravena, A.: IMEX_SfloW2D 1.0: a depth-averaged numerical flow model for pyroclastic avalanches, Geoscientific Model Development, 12, 581–595, 2019.

Delestre, O.: Simulation du ruissellement d'eau de pluie sur des surfaces agricoles, Ph.D. thesis, Université d'Orléans, 2010.

Delestre, O., Lucas, C., Ksinant, P.-A., Darboux, F., Laguerre, C., Vo, T.-N.-T., James, F., and Cordier, S.: SWASHES: a compilation of shallow water analytic solutions for hydraulic and environmental studies, International Journal for Numerical Methods in Fluids, 72, 269–300, 2013.

Dellino, P., Dioguardi, F., Doronzo, D. M., and Mele, D.: The entrainment rate of non-Boussinesq hazardous geophysical gas-particle flows: An experimental model with application to pyroclastic density currents, Geophysical Research Letters, 46, 12 851–12 861, 2019a.

Dellino, P., Dioguardi, F., Doronzo, D. M., and Mele, D.: The rate of sedimentation from turbulent suspension: An experimental model with application to pyroclastic density currents and discussion on the grain-size dependence of flow runout, Sedimentology, 66, 129–145, 2019b.

Dellino, P., Dioguardi, F., Doronzo, D. M., and Mele, D.: A discriminatory diagram of massive versus stratified deposits based on the sedimentation and bedload transportation rates. Experimental investigation and application to pyroclastic density currents, Sedimentology, 67, 2013–2039, 2020.

Denlinger, R. P. and Iverson, R. M.: Flow of variably fluidized granular masses across three-dimensional terrain: 2. Numerical predictions and experimental tests, Journal of Geophysical Research, 106, 553, https://doi.org/10.1029/2000jb900330, 2001.

Diaz, M. J. C., Kurganov, A., and de Luna, T. M.: Path-conservative central-upwind schemes for nonconservative hyperbolic systems, ESAIM: Mathematical Modelling and Numerical Analysis, 53, 959–985, 2019.

Dioguardi, F., Mele, D., and Dellino, P.: A new one-equation model of fluid drag for irregularly shaped particles valid over a wide range of Reynolds number, Journal of Geophysical Research: Solid Earth, 123, 144–156, 2018.

Dufek, J.: The Fluid Mechanics of Pyroclastic Density Currents, Annual Review of Fluid Mechanics, 48, annurev–fluid–122 414–034 252–27, 2015.

Dufek, J., Manga, M., and Staedter, M.: Littoral blasts: Pumice-water heat transfer and the conditions for steam explosions when pyroclastic flows enter the ocean, Journal of Geophysical Research: Solid Earth, 112, 2007.

Dufek, J., Ongaro, T. E., and Roche, O.: Pyroclastic density currents: processes and models, in: The encyclopedia of volcanoes, pp. 617–629, Elsevier, 2015.

Engwell, S., de' Michieli Vitturi, M., Esposti Ongaro, T., and Neri, A.: Insights into the formation and dynamics of coignimbrite plumes from one-dimensional models, Journal of Geophysical Research: Solid Earth, 121, 4211–4231, 2016.

Esposti Ongaro, T., Cerminara, M., Charbonnier, S. J., Lube, G., and Valentine, G. A.: A framework for validation and benchmarking of pyroclastic current models, Bulletin of Volcanology, 82, 1–17, https://doi.org/https://doi.org/10.1007/s00445-020-01388-2, 2020.

Fagents, S. A. and Baloga, S. M.: Toward a model for the bulking and debulking of lahars, Journal of Geophysical Research: Solid Earth, 111, 2006.

Fernández-Nieto, E. D., Bouchut, F., Bresch, D., Diaz, M. C., and Mangeney, A.: A new Savage–Hutter type model for submarine avalanches and generated tsunami, Journal of Computational Physics, 227, 7720–7754, 2008.

Fjordholm, U. S., Mishra, S., and Tadmor, E.: Well-balanced and energy stable schemes for the shallow water equations with discontinuous topography, Journal of Computational Physics, 230, 5587–5609, 2011.

Fyhn, E. H., Lervåg, K. Y., Ervik, Å., and Wilhelmsen, Ø.: A consistent reduction of the two-layer shallow-water equations to an accurate one-layer spreading model, Physics of Fluids, 31, 122 103, 2019.

Ganser, G. H.: A rational approach to drag prediction of spherical and nonspherical particles, Powder technology, 77, 143–152, 1993.

Goutal, N.: Proceedings of the 2nd workshop on dam-break wave simulation, Department Laboratoire National d'Hydraulique, Groupe Hydraulique Fluviale, 1997.

Haider, A. and Levenspiel, O.: Drag coefficient and terminal velocity of spherical and nonspherical particles, Powder technology, 58, 63–70, 1989.

Houghton, D. D. and Kasahara, A.: Nonlinear shallow fluid flow over an isolated ridge, Communications on Pure and Applied Mathematics, 21, 1–23, 1968.

Hyman, D. M., Dietterich, H. R., and Patrick, M. R.: Toward Next-Generation Lava Flow Forecasting: Development of a Fast, Physics-Based Lava Propagation Model, Journal of Geophysical Research: Solid Earth, 127, e2022JB024 998, 2022.

Iga, S.-i. and Matsuda, Y.: Shear instability in a shallow water model with implications for the Venus atmosphere, Journal of the atmospheric sciences, 62, 2514–2527, 2005.

Iverson, R. M. and Denlinger, R. P.: Flow of variably fluidized granular masses across three-dimensional terrain: 1. Coulomb mixture theory, Journal of Geophysical Research: Solid Earth, 106, 537–552, https://doi.org/10.1029/2000jb900329, 2001.

Johnson, C. G., Hogg, A. J., Huppert, H. E., Sparks, R. S. J., Phillips, J. C., Slim, A. C., and Woodhouse, M. J.: Modelling intrusions through quiescent and moving ambients, Journal of Fluid Mechanics, 771, 370–406, 2015.

Johnson, R. S.: A modern introduction to the mathematical theory of water waves, 19, Cambridge university press, 1997.

Keim, B. and de' Michieli Vitturi, M.: Implementation of Vertical Profiles for Velocity and Particle Concentration Into a 2D, Depth-Averaged Model for Dilute Pyroclastic Density Currents, in: AGU Fall Meeting Abstracts, vol. 2022, pp. V52C–0017, 2022.

Kelfoun, K.: Suitability of simple rheological laws for the numerical simulation of dense pyroclastic flows and long-runout volcanic avalanches, Journal of Geophysical Research: Solid Earth, 116, 2011.

Kelfoun, K. and Druitt, T. H.: Numerical modeling of the emplacement of Socompa rock avalanche, Chile, Journal of Geophysical Research: Solid Earth (1978–2012), 110, https://doi.org/10.1029/2005JB003758, 2005.

Kelfoun, K., Samaniego, P., Palacios, P., and Barba, D.: Testing the suitability of frictional behaviour for pyroclastic flow simulation by comparison with a well-constrained eruption at Tungurahua volcano (Ecuador), Bulletin of volcanology, 71, 1057–1075, 2009.

Khezri, N.: Modelling turbulent mixing and sediment process beneath tidal bores: physical and numerical investigations, Ph.D. thesis, School of Civil Engineering, The University of Queensland, 2014.

Kurganov, A. and Petrova, G.: A second-order well-balanced positivity preserving central-upwind scheme for the Saint-Venant system, Communications in Mathematical Sciences, 5, 133–160, 2007.

Kurganov, A., Noelle, S., and Petrova, G.: Semidiscrete central-upwind schemes for hyperbolic conservation laws and Hamilton–Jacobi equations, SIAM Journal on Scientific Computing, 23, 707–740, 2001.

LeVeque, R. J.: Finite volume methods for hyperbolic problems, vol. 31, Cambridge university press, 2002.

Maeno, F. and Imamura, F.: Tsunami generation by a rapid entrance of pyroclastic flow into the sea during the 1883 Krakatau eruption, Indonesia, Journal of Geophysical Research: Solid Earth, 116, 2011.

Mandeville, C., Carey, S., Sigurdsson, H., and King, J.: Paleomagnetic evidence for high-temperature emplacement of the 1883 subaqueous pyroclastic flows from Krakatau Volcano, Indonesia, Journal of Geophysical Research: Solid Earth, 99, 1994.

Mangeney, A., Bouchut, F., Thomas, N., Vilotte, J. P., and Bristeau, M. O.: Numerical modeling of self-channeling granular flows and of their levee-channel deposits, Journal of Geophysical Research, 112, F02 017–21, https://doi.org/10.1029/2006JF000469, 2007.

Marino, B., Thomas, L., and Linden, P.: The front condition for gravity currents, Journal of Fluid Mechanics, 536, 49–78, 2005.

Michel-Dansac, V., Berthon, C., Clain, S., and Foucher, F.: A well-balanced scheme for the shallow-water equations with topography, Computers & Mathematics with Applications, 72, 568–593, 2016.

Murillo, J. and García-Navarro, P.: Energy balance numerical schemes for shallow water equations with discontinuous topography, Journal of Computational Physics, 236, 119–142, 2013.

Neri, A., Esposti Ongaro, T., Cerminara, M., and de' Michieli Vitturi, M.: Multiphase flow modeling of explosive volcanic eruptions, in: Transport phenomena in multiphase systems, pp. 243–281, Springer, 2022.

Oberkampf, W. L. and Trucano, T. G.: Verification and validation in computational fluid dynamics, Progress in Aerospace Sciences, 38, 209–272, 2002.

O'Brien, J. S., Julien, P. Y., and Fullerton, W.: Two-dimensional water flood and mudflow simulation, Journal of hydraulic engineering, 119, 244–261, 1993.

Pareschi, L. and Russo, G.: Implicit–explicit Runge–Kutta schemes and applications to hyperbolic systems with relaxation, Journal of Scientific computing, 25, 129–155, 2005.

Parker, G., Garcia, M., Fukushima, Y., and Yu, W.: Experiments on turbidity currents over an erodible bed, Journal of Hydraulic Research, 25, 123–147, 1987.

Patra, A. K., Bauer, A., Nichita, C., Pitman, E. B., Sheridan, M., Bursik, M., Rupp, B., Webber, A., Stinton, A., Namikawa, L., et al.: Parallel adaptive numerical simulation of dry avalanches over natural terrain, Journal of Volcanology and Geothermal Research, 139, 1–21, 2005.

Pitman, E. B., Nichita, C. C., Patra, A., Bauer, A., Sheridan, M., and Bursik, M.: Computing granular avalanches and landslides, Physics of Fluids, 15, 3638–9, https://doi.org/10.1063/1.1614253, 2003.

Pudasaini, S. P. and Hutter, K.: Avalanche dynamics: dynamics of rapid flows of dense granular avalanches, Springer Science & Business Media, 2007.

Putra, Y. S., Beaudoin, A., Rousseaux, G., Thomas, L., and Huberson, S.: 2D numerical contributions for the study of non-cohesive sediment transport beneath tidal bores, Comptes Rendus Mécanique, 347, 166–180, 2019.

Shimizu, H., Koyaguchi, T., and Suzuki, Y.: The run-out distance of large-scale pyroclastic density currents: a two-layer depth-averaged model, Journal of Volcanology and Geothermal Research, 381, https://doi.org/10.1016/j.jvolgeores.2019.03.013, 2019.

Shimizu, H. A., Koyaguchi, T., and Suzuki, Y. J.: A numerical shallow-water model for gravity currents for a wide range of density differences, Progress in Earth and Planetary Science, 4, https://doi.org/10.1186/s40645-017-0120-2, 2017a.

Shimizu, H. A., Koyaguchi, T., and Suzuki, Y. J.: A numerical shallow-water model for gravity currents for a wide range of density differences, Progress in Earth and Planetary Science, 4, 1–13, 2017b.

Shimizu, H. A., Koyaguchi, T., and Suzuki, Y. J.: Dynamics and Deposits of Pyroclastic Density Currents in Magmatic and Phreatomagmatic Eruptions Revealed by a Two-Layer Depth-Averaged Model, Geophys. Res. Lett., 50, e2023GL104 616, https://doi.org/https://doi.org/10.1029/2023GL104616, 2023.

Sigurdsson, H., Houghton, B., McNutt, S., Rymer, H., and Stix, J.: The encyclopedia of volcanoes, Elsevier, 2015.

Simpkin, T. and Fiske, R.: Krakatau 1883: The volcanic eruption and its effects, Smithsonian Institution Press, 1983.

Sulpizio, R., Dellino, P., Doronzo, D., and Sarocchi, D.: Pyroclastic density currents: state of the art and perspectives, Journal of Volcanology and Geothermal Research, 283, 36–65, 2014.

Toro, E. F.: Riemann solvers and numerical methods for fluid dynamics: a practical introduction, Springer Science & Business Media, 2013.

Valentine, G. A.: Stratified flow in pyroclastic surges, Bulletin of Volcanology, 49, 616–630, 1987.

Von Storch, H. and Woth, K.: Storm surges: perspectives and options, Sustainability Science, 3, 33–43, 2008.

Woods, A. W. and Wohletz, K.: Dimensions and dynamics of co-ignimbrite eruption columns, Nature, 350, 225, 1991.

Woods, A. W., Bursik, M. I., and Kurbatov, A. V.: The interaction of ash flows with ridges, Bulletin of Volcanology, 60, 38–51, 1998.

Zeitlin, V.: Geophysical fluid dynamics: understanding (almost) everything with rotating shallow water models, Oxford University Press, 2018.

Table 1. List of model variables with notation and units.

Symbol	Variable	Units
h	flow thickness	m
B	topography elevation	m
t	time	s
u, v	horizontal velocity components	m/s
T	flow temperature	K
T_a	atmospheric air temperature before entrainment	K
T_b	water vapour temperature before entrainment	K
T_l	water temperature	K
P	ambient pressure	Pa
ρ_m	volumetric averaged flow density	kg/s
ρ_a	air density	kg/s
ρwv	water vapour density	kg/s
ρ_{s,i_s}	i_s solid class density	kg/s
α_a	air volume fraction	
$\alpha_w v$	water vapour volume fraction	
α_{s,i_s}	i_s solid class volume fraction	
C_v	mixture specific heat	$Jkg^{-1}K^{-1}$
C_a	air specific heat	$Jkg^{-1}K^{-1}$
C_{wv}	water vapour specific heat	$Jkg^{-1}K^{-1}$
C_{s,i_s}	i_s solid class specific heat	$Jkg^{-1}K^{-1}$
R_a	air specific gas constant	$Jkg^{-1}K^{-1}$
$R_w v$	water vapour specific gas constant	$Jkg^{-1}K^{-1}$
g	gravitational acceleration	ms^{-2}
g'	reduced gravity	ms^{-2}
E_a	atmospheric air entrainment rate	m/s
E_{wv}	water vapour entrainment rate	m/s
~~D_{s,i_s}~~ S_{s,i_s}	i_s solid class ~~deposition~~ sedimentation rate	m/s
F_x, F_y	friction forces per unit area	$kgm^{-1}s^{-2}$
f	friction coefficient	
ϵ	entrainment air coefficient	
Ri	Richardson number	
$\gamma_{i_s,wv}$	i_s solid class vaporization coefficient	
L_w	water specific latent heat of vaporization	Jkg^{-1}
C_D	gas particle drag coefficient	
Re	Reynolds number	
d_s	particle diameter	m
ν	kinematic viscosity coefficient of atmospheric air	m^2s^{-1}